Computer Vision Based Performance Analysis of Prosthetic Heart Valves

by

Maryam Alizadeh

M.Sc., University of Regina, 2013

B.Sc., Shahid Bahonar University, 2007

A Dissertation Submitted in Partial Fulfillment of the

Requirements for the Degree of

DOCTOR OF PHILOSOPHY

in the Department of Electrical and Computer Engineering

Computer Vision Based Performance Analysis of Prosthetic Heart Valves

by

Maryam Alizadeh

M.Sc., University of Regina, 2013

B.Sc., Shahid Bahonar University, 2007

Supervisory Committee

---

Dr. Alexandra Branzan Albu, Supervisor

(Department of Electrical and Computer Engineering)

---

Dr. Panajotis Agathoklis, Departmental Member

(Department of Electrical and Computer Engineering)

---

Dr. George Tzanetakis, Outside Member

(Department of Computer Science)

## ABSTRACT

Prosthetic heart valves (PHVs) are routinely used to replace defective native heart valves in patients suffering from valvular heart diseases. While PHVs are life-saving, they have limitations in performance and durability. Therefore, it is crucial to rigorously test and evaluate their designs before their implantation. PHVs are commonly examined using cardiovascular testing equipment that measures the hemodynamic characteristics of the valves, while also providing the opportunity for their visual assessment by collecting high-quality videos. Such visual data, obtained during mechanical simulations, are typically assessed by human experts, which is a tedious and error-prone task. Automatic assessment of PHVs from video data is possible, however, there are some challenges that need to be addressed. The evolution of the valve orifice area during one cardiac cycle is one of the key quality metrics for PHV visual assessment. Very fast motion of the valve's leaflets is one of the challenges while dealing with the visual data. Nevertheless, the more important issue lies in the orifice being partly occluded by the inner side of the leaflets or inaccurately depicted due to its transparency. This issue has not been addressed in the literature.

In the first part of the thesis, a novel orifice area segmentation algorithm is proposed for automatic quantitative performance analysis of PHVs, based on the leaflet free edges to accurately extract the actual orifice area. The video frames, recorded by a high-speed digital camera during *in vitro* simulations, are used to obtain an initial estimate of the orifice area using active contouring methods. This initial estimate is then refined to detect leaflet free edges via a curve extension scheme and considering brightness and smoothness criteria. Both of the developed algorithms are later modified for addressing challenges related to the fast motion of leaflets, automatic detection of the beginning of a cycle, and overly bright spots and narrow areas. Evaluation on several cases including three different PHVs and with different video

qualities demonstrated the effectiveness of the proposed approach and adjustments in detecting valve leaflet free edges and extraction of the actual orifice area. The proposed method significantly outperforms a baseline algorithm both in terms of valve design and computer vision evaluation metrics. It can also cope with lower quality videos and is better at processing frames with a very small opening, which is a very crucial quality for determining the malfunctions related to improper closing of the valves.

In the second part of the thesis, the above-mentioned segmented orifice area is used for the durability estimation of the prosthetic heart valves. More than 50% of PHVs encounter a structural failure within 15 years post-implantation mostly because of the excessive localized forces on some areas. We perform a computer vision (CV)-based analysis of the visual symmetry of valve leaflet motion and investigate its correlation with the functional symmetry of the valve. We hypothesize that an asymmetry in the valve leaflet motion will generate an asymmetry in the flow patterns, resulting in added local stress and forces on some of the leaflets. Two pair-wise leaflet symmetry scores are proposed based on diagonals of orthogonal projection matrices (DOPM) and dynamic time warping (DTW) techniques.

The proposed symmetry score profiles are compared with fluid dynamic parameters (vorticity and velocity values) at the leaflet borders, obtained from valve-specific numerical simulations. Experiments on four cases including different tricuspid PHV designs yielded promising results, with DTW scores showing good coherence with respect to the simulations, which confirms our hypothesis. The established link between visual and functional symmetry opens the door for durability estimation of prosthetic heart valves using computer vision techniques.

# Contents

# List of Tables

# List of Figures

# ACKNOWLEDGEMENTS

I would like to express my deepest gratitude to my supervisor, Professor Alexandra Branzan Albu for her continued support, guidance, and invaluable insight. My sincere appreciation goes to Dr. Mélissa Côté, for her assistance and thoughtful and detailed feedback. I am fortunate to have been part of CVLab at the University of Victoria, thank you Alireza, Amanda, Alex, and Tunai, I enjoyed working and exchanging ideas with you. In addition, I gratefully recognize the help of ViVitro Labs Inc experts, especially Rob Fraser and Joe McMahen for sharing data and their experience with me.

# DEDICATION

I dedicate my dissertation to:

My parents, who never stop giving of themselves in countless ways,

My loving husband, Ahmad, who has always been source of support and encouragement, and

My handsome son, Sahand, whose smiles give me the power to become a stronger and better version of myself.

Thank you, my love for you all can never be quantified.

# Chapter 1

# Introduction

## 1.1 Background and Motivation

According to World Health Organization (WHO), heart disease is the number one cause of death in the world [1], which is primarily caused by the malfunction in one or more of the four heart valves (Figure 1.1). In Canada, more than 90 thousands death are recorded, yearly, due to heart diseases [2]. In the United States alone, more than 5 million people are diagnosed with valvular heart disease each year [61]; these numbers will most likely increase due to longer life expectancy. In fact, around 10% of the 75 years and older population suffer from degenerative abnormalities associated with at least one of the heart valves [66]. One of the well-developed and efficient therapeutic options for this group of patients is to replace the dysfunctional valve with a prosthetic heart valve, which has properties that are most similar to the native heart valve.

The ideal heart valve implant should function in coordination with the rest of the circulatory system to protect each part from damage. It should provide long-term durability without causing any dangerous side effects for the patient's health. The valve's hemodynamic performance -which describes the flow of blood through the

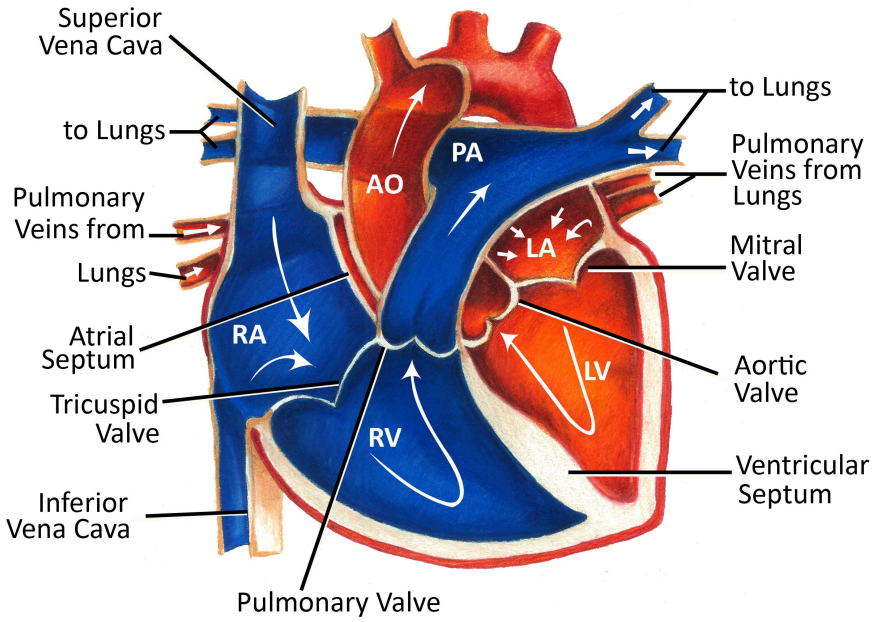


Figure 1.1: Schematic of the heart anatomy. Image taken from *pediatricheartspecialists.com*

heart valve- affects the quality of patient's life immediately after implantation and through their lifetime [61, 76]. There are two general types of prosthetic heart valve implants: mechanical and biological heart valves (Figure 1.2). The type of valve used for each patient depends on their health condition, age and life expectancy, medications, and lifestyle.

Mechanical valves are mostly made of strong materials; therefore, they are the most long-lasting form of heart valves. Usually, they last throughout the remainder of the patient's life and there is no need for reoperation to replace them. However, because of their opening and closing mechanism, the mechanical valves might create water hammer effect, regurgitation jet flow and cavitation [86, 20, 90]. This can result in blood cell damage, thrombosis and thromboembolism [50, 33]. To overcome these issues, the patient should be on anticoagulant medication for the remainder of their

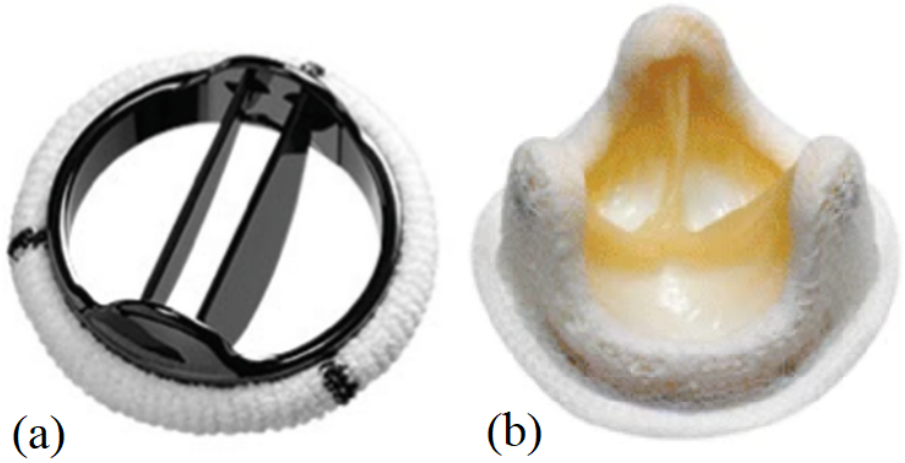


Figure 1.2: Examples of (a) mechanical [54] and (b) biological [45] heart valves.

life, which might also increase the risk of bleeding due to overly thinned blood.

Unlike mechanical valves, biological heart valves have very similar behavior to the native heart valves [56], due to their similarity in the tissues and number of leaflets. Therefore, there is less concern regarding the blood flow turbulences resulting in blood cell damages and other similar health issues and consequently, there is no need for long-term use of medication. However, there are other issues that make these types of valves less reliable. Tear and calcification (caused by the design of the valve and the resulted stress on the leaflets) are two of the main factors and they increase the possibility of reoperation to change the implanted heart valve within 15-20 year period [68, 72]. Researchers are actively working on new designs for more reliable and durable heart valves.

The quality of the implanted heart valve has a direct impact on its durability hence the patient's quality of life. It is critically important to ensure optimal characteristics of a prosthetic valve before its implantation in the human body. There are several quality parameters, which are defined during the course of developing different types of heart valves, to evaluate the performance of a prosthetic heart valve by comparing them with those of a native valve. The flow and pressure data of the fluid

passing through the valve -in various stages of durability test- is one of the factors that determine the quality of the valve. It is also common to visually assess the performance of the heart valve in either *in vivo* or *in vitro* environments. Visual data (images/videos) are collected while the heart valve is in function and an operator ranks the performance of the valve, amongst several pre-defined levels, by comparing them with the ideal native heart valve. The visual assessment provides the opportunity of studying some quality parameters (such as the opening area of the valve and opening and closing intervals) that cannot be verified otherwise; however manual assessment by an operator is prone to human error and personal judgment of the operator, for example in determination of the ranking level that the valve belongs to. Therefore, it is of great interest to develop approaches for automatic visual analysis of heart valves.

ViVitro Labs, Inc. based in Victoria, BC, is one of the companies that develop cardiovascular device testing equipment. Their equipment is used in R&D and educational facilities. Their *Pulse Duplicator system* is the world's most widely cited and most used *in vitro* cardiovascular hydrodynamic testing system [41]. The pulse duplicator (Figure 1.3) simulates the function of half of the human's heart, while the prosthetic heart valve can be mounted in the model. It generates pulsatile flow through the heart valve and the flow and pressure sensors, before and after the heart valve, measure and collect the flow data during each experiment. The other testing device, developed by ViVitro, is *HiCycle Durability Tester*, which can be cycled at accelerated rates up to 1650 cycles/minute (comparing to 70 cycles/minute, human's usual heartbeat rate), and provides the opportunity of verifying the durability of the heart valve, during its whole expected lifetime, in a much shorter period of time. Pulse duplicator and HiCycle durability tester are also equipped with a high-quality digital camera capable of recording high frame rate and shutter speed videos. These

Figure 1.3: Pulse Duplicator system, ViVitro Labs Inc.[41]

high-quality videos can be used for visual assessment of the heart valve in addition to flow data measurements. Figure 1.4 shows three example frames of the test video, recorded from a bioprosthetic heart valve, in its opening phase, while in function in the pulse duplicator system. This study will use these high-quality imagery data for purpose of performance analysis of prosthetic aortic heart valves. We will focus on the opening area of the valves, propose approaches for their accurate segmentation and investigate and analyze their evolution over the whole cardiac cycle.

## 1.2 Contribution

The outcome of this thesis contributes to the advancement of knowledge in both theoretical and practical aspects. In the first part of the thesis (Chapters 3 and 4),

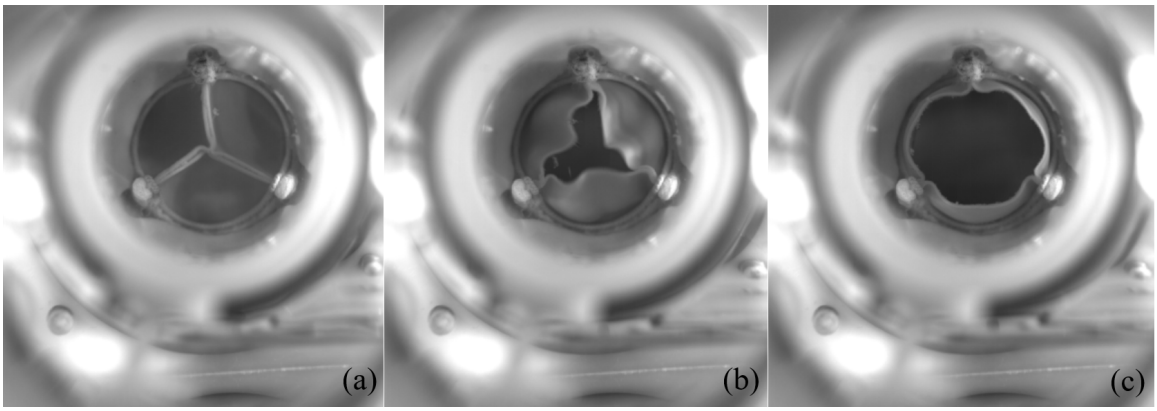


Figure 1.4: Example frames from a test video acquired from an aortic bioprosthetic heart valve, in opening phase, in pulse duplicator system; (a) valve closed, (b) partly open, and (c) completely open.

a new 2D curve extension scheme is proposed based on brightness and smoothness criteria. It allows for recovering the true shape of the border of the leaflets when deformable models typically fail due to visible inner regions of the underlying object. From a practical point of view, the application of the proposed scheme to the problem of detecting and tracking the free edges of PHV leaflets will enable the automatic analysis of prosthetic heart valves performance from high-speed video recordings.

In the second part (Chapter 5), we propose to utilize visual symmetry information derived from the shape of pair-wise valve leaflet motions to perform PHV analysis via two different symmetry scores. Furthermore, we evaluate the geometric symmetry of the valves in comparison with the functional symmetry from a fluid dynamics numerical model. From a practical point of view, we further facilitate PHV durability estimation by using CV methods and linking visual and functional symmetry. The review of the related research work in the next chapter will shed the light on the importance of the proposed techniques and how they fill the existing knowledge gap in the performance analysis of prosthetic heart valves.

The work described in this thesis has also resulted in three peer-reviewed articles on:

1. Leaflet free edge detection for the automatic analysis of prosthetic heart valve opening and closing patterns from high-speed video recordings [6].

2. Automatic segmentation and tracking of biological prosthetic heart valves [7].

3. Towards durability estimation of bioprosthetic heart valves via motion symmetry analysis [8].

I was the first author of all the papers. The co-authors helped and supervised the process of writing and revising the manuscripts, literature review, and their submissions.

## 1.3 Structure of the Thesis

In the next chapter, the main body of related work will be reviewed, the knowledge gaps and the research needs will be discussed and the research objectives will be defined accordingly. In Chapter 3, the details of the proposed method for detection and tracking of the free edge of leaflets are presented and evaluated. In Chapter 4, several modifications are proposed to enhance the robustness, reliability, and applicability of the developed methods. Chapter 5 presents the method for visual symmetry analysis of the prosthetic heart valves and evaluates the proposed method in comparison with the functional symmetry of the valves obtained via numerical modeling. Discussion on key findings and suggestions for future work are summarized in Chapter 6.

# Chapter 2

# Literature Review and Problem Definition

This chapter overviews the literature related to different aspects of this proposed research, i.e., performance evaluation of prosthetic heart valves. The first part focuses on different methods of data acquisition and the second section reviews the approaches for processing and interpreting the data. Finally, in light of the reviewed literature, we will state our research problem(s) along with a discussion of associated challenges. We will also present our research objectives.

## 2.1 Data Acquisition

### 2.1.1 Mechanical and Numerical Simulations

Generally, there are two main paradigms used in previous related research for simulating the performance of prosthetic heart valves: numerical and mechanical (physical) simulations. Some studies use numerical solutions for predicting the behavior and dynamics of the heart valve in interaction with the blood flow [24, 49, 89, 10, 62]. For

example, Choi et al. [24] proposed a finite element analysis model to simulate the fluid-structure interaction in order to investigate mechanical heart valve hemodynamics and leaflet dynamics. As the numerical simulations can be associated with the various numerical approximations and parameter estimations, they might not be able to reproduce the reality of the heart valves accurately and efficiently, nevertheless, they could be very informative as complementary evaluation approaches.

As real-life accuracy of results is vital for patient's life and health, one might prefer mechanical simulation methods, as they evaluate the performance of the heart valves in the environment identical or very similar to their physiological setting. In context of mechanical simulations, Grigioni et al. [38] studied several technologies for so called *in vitro* measurements, to measure both hydraulic and fluid dynamic parameters of heart valves. They suggested these measurements provide an effective indication of the performance of the heart valves and determine their degree of functionality and, to this day, they are mainly used for evaluation of prosthetic heart valves. Mechanical simulation itself can be divided into *in vivo* and *in vitro* categories. Each of these categories requires different methods of data acquisition and measurements, which will be discussed in more detail in following sections.

### 2.1.2 Imaging Modalities

Mechanical simulations benefit from not only measurement of flow and pressure data, but also from the possibility of visual data acquisition and analysis. Availability of the captured images/videos of the heart valves enables measurement of some quantitative assessment criteria (e.g., valve opening area) in addition to a qualitative evaluation of the dynamic behavior of the heart valves. Different image acquisition methods were suggested in the literature.

Ultrasound and fluoroscopy are two of the traditional techniques, used for *in vivo*

assessment of the heart valves [57, 78]. More recently, the Magnetic Resonance Imaging (MRI) and Computed Tomography (CT) have been suggested for both *in vivo* and *in vitro* measurements [75, 22, 29, 11, 12]. In 2011, von Knobelsdorff-Brenkenhoff et al. [81] proposed a Cardiovascular Magnetic Resonance (CMR) tool in order to visualize the intravascular flow dynamics and to manually determine the prosthetic orifice area. The proposed approach can be used for both *in vitro* and *in vivo* measurements. Habets et al. [39] studied the manually *in vivo* measurement of the valve's closing and opening angles using the Computed Tomography Angiography (CTA). In 2015, Suchá et al. [74] presented a more comprehensive review of multimodality imaging assessment of prosthetic heart valves. They overviewed the potentials and pitfalls of CT and MRI as complementary method to Echocardiography in assessment of the prosthetic heart valves. They found that CT complements Echocardiography in detecting tissue related issues such as obstruction causes, calcification and endocarditis extent while MRI is helpful in providing information on flow patterns and velocities.

### 2.1.3 High-Speed Digital Cameras

Another alternative for acquiring visual data, within the *in vitro* environment, is to use the high-speed digital cameras. The high quality of the recorded images and videos with availability of the high frame rates and shutter speeds enables us to investigate the behavior of fast-moving objects such as the valve's leaflet opening and closing pattern in great detail [44]. The possibility of capturing high quality images/videos from different angles encouraged many researchers to utilize these high-speed cameras in conjunction with the computer vision techniques in order to improve or automate the evaluation process [73, 30]. In the following section, several of these techniques will be reviewed in more detail. The focus will be on how they use different approaches for measuring the flow and pressure data and for studying the opening and closing

patterns and other kinematic behaviors of the heart valves.

## 2.2 Video Data Analysis

### 2.2.1 Particles, Laser Dots and Markers

Because of the limitations in availabilities of high-quality cameras, earlier research works mostly relied on using external markers, markers or particles, to facilitate the process of the visual data analysis. In 1989, Affeld et al. [4] suggested the use of an enlarged model of the artificial heart valve in combination with added small plastic spheres to the apparatus in order to measure the streamline and velocity profiles by comparing the two consecutive frames. The enlarged model reduces the velocity and thus allows for a more detailed analysis. Brücker et al. [15] used a similar technique for analyzing the pulsatile flow through a three leaflet heart valve by computing cross-correlation between consecutive frames and using Digital Particle Image Velocimetry (DPIV). They added small fluorescent tracer particles to the working fluid and illuminated them by a laser beam. Additionally, in order to measure the opening angle, they manually marked the tips of valve leaflets and tracked them using image processing techniques. Lu et al. [53] also used DPIV method for measurement of flow characteristics (e.g. velocity and vorticity fields) in artificial monoleaflet, bileaflet and trileaflet heart valves.

Gao et al. [37] proposed the use of two cameras to investigate the motion of valve's leaflets by 3D reconstruction of leaflet surfaces. They marked the leaflets with several India ink dots and applied Dual Camera Stereo Photogrammetry (DCSP) to triangulate two images of the same marker and thus obtain a set of 3D coordinates of marked points on the leaflets. These 3D coordinates were then used in a patch-based surface fitting mechanism to reconstruct the leaflet surface. They suggest that this

method helps to recognize the uneven distribution of the mechanical stresses occurring in the leaflet motion, which results in the long-term failure of prosthetic heart valves. On the other hand, their approach had the disadvantage of obstructed markers due to leaflet motions; therefore, reconstruction of the leaflet surface might not be possible in every frame of the video. To address the issue of obstructed markers, Iyendgar et al. [42] suggested the 3D reconstruction of leaflet surfaces by using a non-contacting structured laser light projection technique. They projected a matrix of laser light points over the entire leaflet surface and tracked them, at discrete temporal instances, by a stereo system of high-resolution borescopes. Lu et al. [53] tracked reflective dots markers on the leaflets to study the valve closing mechanisms. Due to limitations of the apparatus shape and the use of a single camera, this approach was not able to successfully obtain the full temporal variations of the angular velocity.

Recent advancements in digital cameras, more specifically the availability and affordability of high-speed digital cameras provided the researchers with a unique opportunity to acquire high-quality visual data, which enabled them to evaluate the performance of heart valves with no need of using additional markers and particles. They are now able to use computer vision and image processing methods that focus on the original pixel intensities, such as digital kymography, thresholding and deformable models. The following section describes these approaches in more details.

### 2.2.2 Digital Kymography

Digital kymography allows for the visualization of changes in the image in a compact manner by plotting extracted (or projected) image lines along a time axis. Friedl et al. [35] used this method to determine the performance of the artificial heart valves by comparing the opening and closing intervals of the artificial and native heart valves. Figure 2.1 shows the procedure of generating a kymogram from a sequence of frames.

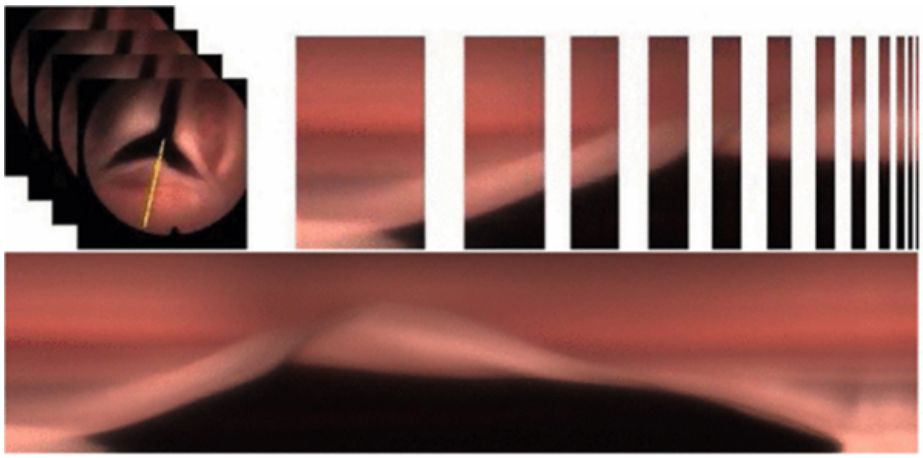

Figure 2.1: Generation of digital kymograms from endoscopic heart valve video recording. Top: definition of the kymogram line (yellow line) and concatenation of the extracted lines; bottom: final digital kymogram of a native heart valve. Adapted from Friedl et al. [35].

The pixel values along the yellow line (from each frame) are concatenated and plotted in Y axis of a 2D plot VS temporal evolution of the video (X axis).

Their technique automatically segmented the orifice area by thresholding the obtained kymogram. Because of lack of the spatial calibration within the available videos, they computed normalized orifice distances, which allowed for valve comparisons but not for absolute measurements. Kondruweit et al. [48] also used digital kymography in combination with cardio-vibrogram for visualization of the opening and closing procedures. Despite the capability of the digital kymography, this technique focuses on a very local region of the valve and therefore cannot provide a complete overview of the whole valve's motion.

### 2.2.3 Thresholding

Thresholding converts a grayscale image to a binary one based on a threshold intensity value. Hahn et al. [40] proposed three different variations of thresholding in order to segment the orifice area of a trileaflet heart valve. The first approach simply generates

a binary image by using a user-defined threshold value. The other two approaches use the Otsu's method and finite mixture models to automatically derive the threshold value. To achieve accurate segmentation result from thresholding, the area of interest should have homogeneity in terms of gray level values; however, this is not the case in many images/frames. In practice, it is rather difficult to achieve a homogeneous background against which to project the orifice [26].

### 2.2.4 Deformable Models

Defining the orifice area as the area surrounded by the borders of valve leaflets and delineating the leaflet borders is more complex yet more accurate approach for orifice segmentation. Since the leaflets move freely, the area enclosed by them may form a variety of shapes, which cannot be known in advance. Therefore, deformable models can be a good option for finding this deformable area.

Deformable models are 2D curves or 3D surfaces, defined within an image domain. The models can change shape by minimizing the combination of internal and external energies within the image domain. Internal forces keep the model smooth during deformation while external forces, which are computed from the image data, move the model toward desired object boundaries [77, 87]. The deformable models exploit constraint from images (or video frames) and may incorporate prior knowledge on the structures present in the image, which makes this approach robust against image noise and boundary gaps.

Wittenberg et al. [85] proposed the implementation of the snakes (active contours) technique, which is a popular type of deformable model, to study and calculate the orifice area of the (explanted pig) heart valve and its geometric evolution over time. They manually initialize the snake by drawing a freehand form of an initial starting contour into a frame with an open orifice. They also apply local constraints to three

nodes of the contour by manually selecting the three commissions between the leaflets. Kondruweit et al. [47] proposed a combination of the digital kymograms and snakes for the study of the behavior of explanted pig heart valves. Digital kymograms were calculated at various angles (over the manually drawn kymogram lines) to analyze the different closure phases, while the snake was implemented to calculate the orifice area over time using the same technique as [85].

Condurache et al. [26] proposed an automatic method for initialization of the snake and segmentation of the orifice area. They applied their approach on videos captured during *in vitro* mechanical simulations and compared their results with the ones obtained via different methods of thresholding, similar to those of [40]. They automatically located the anchor points (commission points) to generate the initial contour and also to define attractors for better detection and tracking of the leaflet boundaries. Figure 2.2 shows the defined attractors around the anchor points (black arcs) and the resulted segmented orifice area, by implementing the snake method, with and without the attractors. They argued that the use of attractors makes the snake robust for locating the actual border of the leaflets in the areas where the contrast between the boundaries and the background is not distinguishable. This approach resulted in an accurate segmentation of the orifice area despite the lack of brightness homogeneity in the opening area and/or background - unlike the investigated thresholding approaches.

In 2009, Condurache et al. [27] completed their study of the heart valves by analyzing the fluttering of the leaflets both in time and space. The borders of leaflets were achieved using their proposed approach in [26]. Fluttering, in time domain, was detected as a high-frequency signal superimposed on the orifice curve (curve representing orifice area VS time). To quantify the detected fluttering, the mean energy of the signal in the high-pass part of the spectrum was computed.

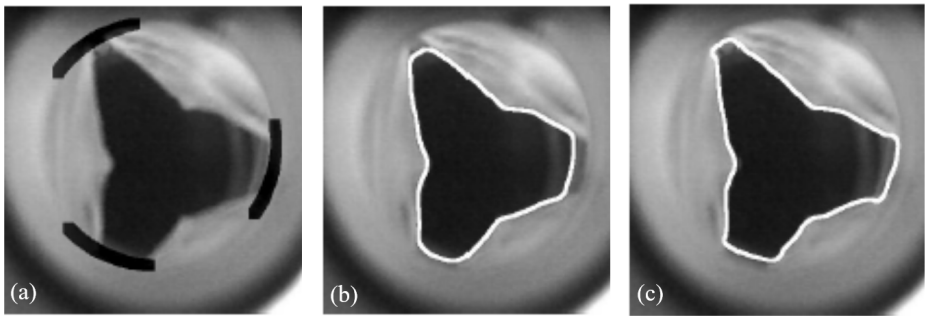


Figure 2.2: (a) An example frame superimposed by the defined attractors (black arcs), (b) segmented orifice area (white contour) by implementing the snake method without attractors, (c) with attractors [26].

## 2.3 Performance Measures

### 2.3.1 Heart Valve Assessment Metrics

Different measures have been introduced during previous research works in order to quantify the performance of the heart valves based on visual data analysis. These quality parameters can be related to the flow characteristics or the heart valve opening and closing behaviors. Lu et al. [53] measured velocity fields and vorticity distributions by using DPIV technique and investigated their effect on closing mechanism of the heart valve. They found that the uniformity of the velocity profiles and vector fields ensures that there are no strong turbulence vortices in reverse direction. The reverse flow accelerates the leaflet movement and applies additional pressure which results in unnatural leaflet closure and generation of water hammer effect. They also measured the closing angle of leaflets as the larger angle in the closing phase results in a higher closing velocity and generates stronger reverse flow. Gao et al. [37] also studied the distribution of mechanical stress over the leaflet surface during opening and closing phase of the valve cycle by 3D reconstruction of leaflet surfaces. They concluded that the uneven distribution of the mechanical stress results in failure of bioprosthetic heart valves.

Friedl et al. [35] focused on the opening and closing intervals of the heart valves as they have direct effect on the optimal blood flow. They provided a quantitative measure for evaluating the performance of the implanted heart valve by comparing the opening and closing intervals to those of a native heart valve. Another group of studies have focused on the opening area of the heart valve and its evolution during a valve cycle. Condurache et al. [26, 27] quantified the heart valve performance by measuring the orifice area over time (in each frame of the video test), and thus by creating an *orifice curve*. This function helps to compute several other measures such as the maximum opening area and when (in which frame of the valve cycle) it happens, how fast the valve opens and closes (opening and closing intervals) and the overall trend of the valve evolution during all phases of a cycle. Figure 2.3 shows a typical orifice curve and the evolution of the opening area during the valve cycle. In addition to the orifice area, fluttering of the valves was also measured. The research relates the fluttering to the major stress on the leaflets, which is likely to reduce the durability of the implants and to consequently affect the health of the patients [27, 80, 36].

Among the reviewed research works, the approach proposed by Condurache et al. [27] appears to be the most promising automated method as it provides the most comprehensive quality assessment by measuring the orifice area during the test sequence. However, there are several aspects of their method that requires further modifications, to be applicable for efficient quality control of the heart valves. One of the difficulties is that their proposed method is not capable of fully detecting and tracking the free edges of leaflets. In some cases, the opening area is occluded by the valve's leaflets or inaccurately depicted due to visible inner side of valve region (Figure 3.1). This study aims to address these issues by developing an automated method for tracking free edges of leaflets separately and not as borders of the segmented orifice

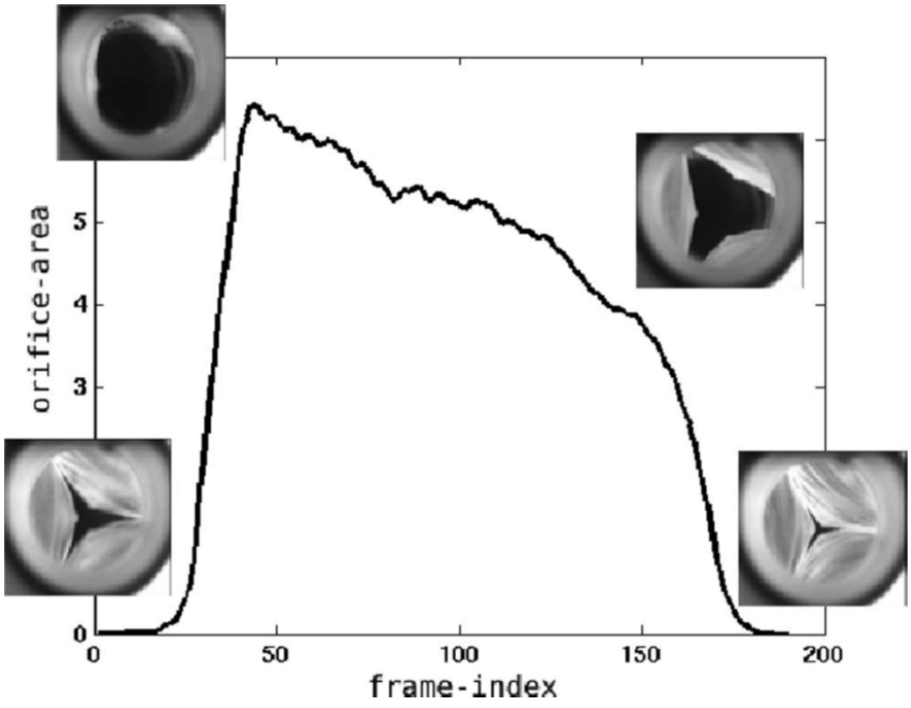


Figure 2.3: A typical orifice curve illustrating the evolution of the orifice area during a valve cycle, [27].

area (Chapter 3 and 4).

### 2.3.2 Symmetry Assessment Metrics

Having orifice area of the prosthetic heart valve for one cycle, one could study some other kinematic behavior of the valve. Fluttering of the leaflets is one of the parameters that have been investigated in several research work [40, 27, 34]. The other quality parameter, that is of interest to this thesis, is symmetry of the orifice area or symmetry of the valve leaflets in motion, which can be translated to symmetry in PHV performance. To the best of this author's knowledge, visual symmetry of the prosthetic heart valves has not been investigated previously in the literature. However, the importance of symmetry and uniformity of the flow pattern has been studied and its impact on durability of the PHVs have been demonstrated [53, 37, 82].

Therefore, one could investigate the relation between visual symmetry of the PHVs in motion and the symmetry of the hemodynamic characteristics of the valve. In the following, the related work to symmetry assessment is presented.

Symmetry, in the general sense, expresses the notion that a structure is made from multiple copies of the same smaller unit. More formally, symmetry is examined via the effect of transformations on the structure in a certain space such that its sub-parts map to each other [51]. In the 2D Euclidean space, there are four types of elemental symmetries: reflection, rotation, translation, and glide reflection. In CV, research on symmetry has mostly focused on reflection symmetry, with an increasing awareness of the entire symmetry spectrum [51]. Techniques for measuring symmetry in visual data can be divided into global and local; local techniques can be further divided into area- and feature-based.

Global techniques are generally based on applying certain types of transforms to search for symmetry axes [84]. For instance, Derrode and Ghorbel [28] used the Fourier–Mellin transform for symmetry detection in gray level objects, Shen et al. [71] developed a unified method for detecting reflection and rotation symmetry in 2D images based on generalized complex moments, and Kondra et al. [46] proposed multi-scale kernel operators for reflection and rotation symmetry detection in real-world scene images. Global techniques, which consider information derived from entire images, can characterize all potential symmetries but are typically less efficient than local techniques.

Area-based local techniques are among the easiest ones to implement but do not consider shape-related information. In general terms, maximal symmetry happens when two areas completely match, for instance via convolution or area ratio computations. Most area-based works come from medical image registration applications [64, 60, 65]. Moyer et al. [59] and Eder et al. [32], in similar studies, evaluated breast

symmetry of the patients pre- and postoperatively by comparing their reconstructed 3D surfaces.

Feature-based local techniques consider higher-level information embedded in the shape, contour, and/or other key features of images. They use feature descriptors and rely on information extracted from pixel intensity, pixel intensity changes, contour shapes, etc. In one of the early papers, Reisfeld and Yehezkel [64] proposed to use gradient information to detect facial features via generalized symmetry. Their symmetry score compared the gradient intensity and orientation between two points. Some of the feature descriptors rely on the intensity of the pixels. One of the well known and widely used descriptors from this category is SIFT (Scale Invariant Feature Transform) descriptor. SIFT and its variants have been used for symmetry detection and evaluation applications [23, 67, 21, 52, 63], however their reliance on the pixel intensity values make them vulnerable to noise and illumination changes.

The other sub-category of feature descriptors focuses on the silhouette and contour of the areas in the image. Atadjanov and Lee [13] proposed a descriptor for reflection detection by focusing on the edges and the key points of the contour where the curvature of the edge becomes a local extremum. Wang et al. [84] established the correspondence of locally affine invariant edge-based features to detect single and multiple reflection symmetry axes in synthetic and real-world images. Their approach relied on diagonals of orthogonal projection matrices (DOPM) as contour descriptors for contour matching, invariant to the full set of affine transformations [83].

Another group of approaches for object and contour matching is calculating their distances, e.g., Hausdorff distance [31]. Fréchet distance has also been used for contour matching applications [9, 16]. It considers the location and ordering of the points on the curves and measures the similarity between them. Shahbaz [69] studied several variants of Fréchet distance for different situations of contour matching (e.g., partial

contour matching). However, it has been shown that Fréchet distance is sensitive to noise and outliers [5, 88], as it calculates the maximum distance between the corresponding points on the curves. On the other hand, Dynamic Time Warping (DTW) -which is very closely related to Fréchet distance- finds the optimal matching points on the two curves and calculates the summation of the absolute distances between them, which makes it a more robust approach. DTW has been originally used for comparison of temporal sequences, but its applications expanded to many other areas including curve matching and symmetry detection [88, 3, 25].

Of all the reviewed symmetry detection and curve matching methods, DOPM descriptor and DTW techniques seem to be more inspiring and applicable to this study's cases and available dataset. The details of the main problems that are of interest to this dissertation are discussed in the following.

## 2.4 Problem Statement

In the reviewed literature, the importance of accurate and efficient performance evaluation of PHVs was highlighted. A quantitative analysis of videos enables us to study qualitative parameters, such as those related to evolution of the valves' orifice area over time (orifice curve), their opening and closing motion patterns and their leaflet kinematics including fluttering and symmetry of the valve's leaflets in motion. The accurate segmentation of the orifice area and the visual symmetry analysis of the orifice area are our main topics of focus.

1- Segmentation of the orifice area have been studied in the literature, however there are some challenges that need to be addressed. One difficulty comes from the fast motion of the valve's leaflets during the opening and closing phases, which results in blurry edges. But the major issue is the orifice area being partly occluded

by the inner side of the leaflets or inaccurately depicted due to its transparency. Segmentation methods based on thresholding, shape priors, and deformable models (e.g., active contours), typically fail to segment and extract the boundaries of the valve leaflets under those conditions. Therefore, the border of the segmented orifice area does not necessarily represent the free edges of leaflets. Inaccuracy in locating and tracking the leaflets' free edges results in erroneous determination of the orifice curve, which is a crucial parameter for PHV design assessment. In addition, the contour of this detected orifice area would be used to determine if the leaflets ever come in contact with the stent of the valve, and also to investigate the symmetry of the leaflet's movement.

2- Although uniformity and symmetry of hemodynamic characteristics of the PHVs are vastly studied and their effect on durability of the heart valves are demonstrated in the past studies, the visual symmetry of the heart valves in motion has never been investigated. Considering the potential link between visual symmetry and functional symmetry of the PHVs, visual symmetry analysis of prosthetic heart valves can provide a unique opportunity for their performance evaluation and durability estimation using computer vision techniques, as an alternative to current manual, user-oriented and time-consuming approaches.

## 2.5 Objectives

The above-mentioned problems and knowledge gaps define the global objective of this research as developing automatic, accurate and efficient computer vision frameworks for quantitative performance analysis of biological PHVs, from video footage acquired during *in vitro* testing. The specific objectives are defined as:

1. Developing an approach for detection of free edges of leaflets from high-speed

videos for the purpose of automatic analysis of PHVs

2. Further improvements and modification of such developed method to broaden its applicability and enhance the performance accuracy.

3. Analyze and quantify the visual symmetry of the valves' leaflets in motion in comparison with functional symmetry to investigate potential correlation between them for the purpose of durability estimation of the PHVs.

# Chapter 3

# Leaflet Free Edge Detection from High-Speed Video Recordings

This chapter focuses on the detection and tracking of the free edge of leaflets in prosthetic heart valves. For this purpose, two main algorithms are developed. The first algorithm performs segmentation of the orifice area by using active contours (Section 3.1). The second algorithm (Section 3.2) detects the leaflet free edges, by refining the shape of the segmented orifice area, and allows us to address cases for which the orifice is partially occluded by the inner side of the valve's leaflets (Figure 3.1).

In Section 3.3, the experimental results are presented, and their accuracy is evaluated by comparing them with a baseline method and the ground truth data. The extracted information can be used to determine several quality parameters, such as how fast the valve opens and closes, how long the valve stays open, as well as the maximum opening of the valve, which constitute crucial data for assessing the opening and closing patterns of PHVs.

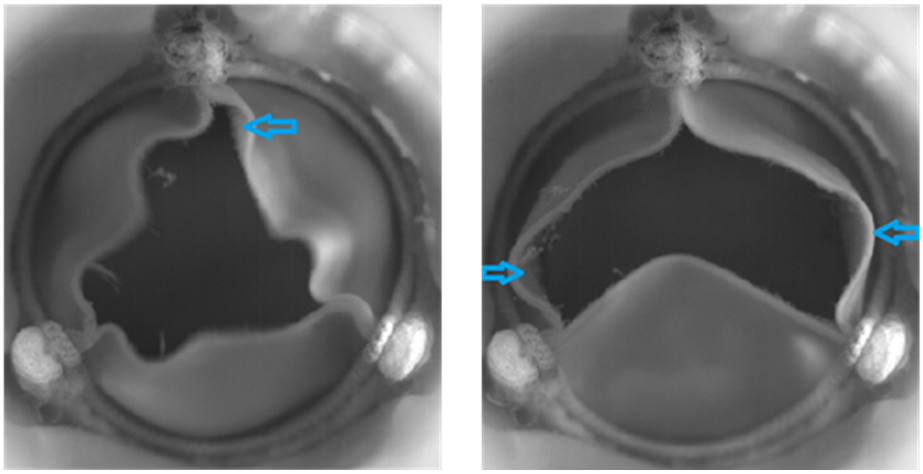

Figure 3.1: Example frames in which the orifice area is partially visually bordered by the inner side of the leaflets (blue arrows) instead of the free edges of the leaflets.

## 3.1 Orifice Area Segmentation

The orifice area segmentation algorithm has been summarized in Figure 3.2 (top). First, pre-processing is carried out to determine the region of interest (ROI) inside the frames and obtain the initial approximation (mask) of the orifice area. The orifice area is then segmented either via active contouring, initialized using the initial mask or via thresholding depending on where the valve is in its opening and closing cycle (trigger). This first algorithm builds upon the method proposed in [27] but differs on several levels. Although the general idea of the pre-processing steps is similar, the way to select the final ROI and the construction of the mask differs. The trigger part was also absent from [27].

### 3.1.1 Pre-processing

Knowing the actual radius of the imaged PHV, an ROI that corresponds to the inside of the circular outline of the valve is first determined via circular Hough transform [14] applied on a Canny edge map of the frame (Figure 3.3 a-b). A frame showing a small opening of the valve (akin to a three-pointed star shape) is preferred. The

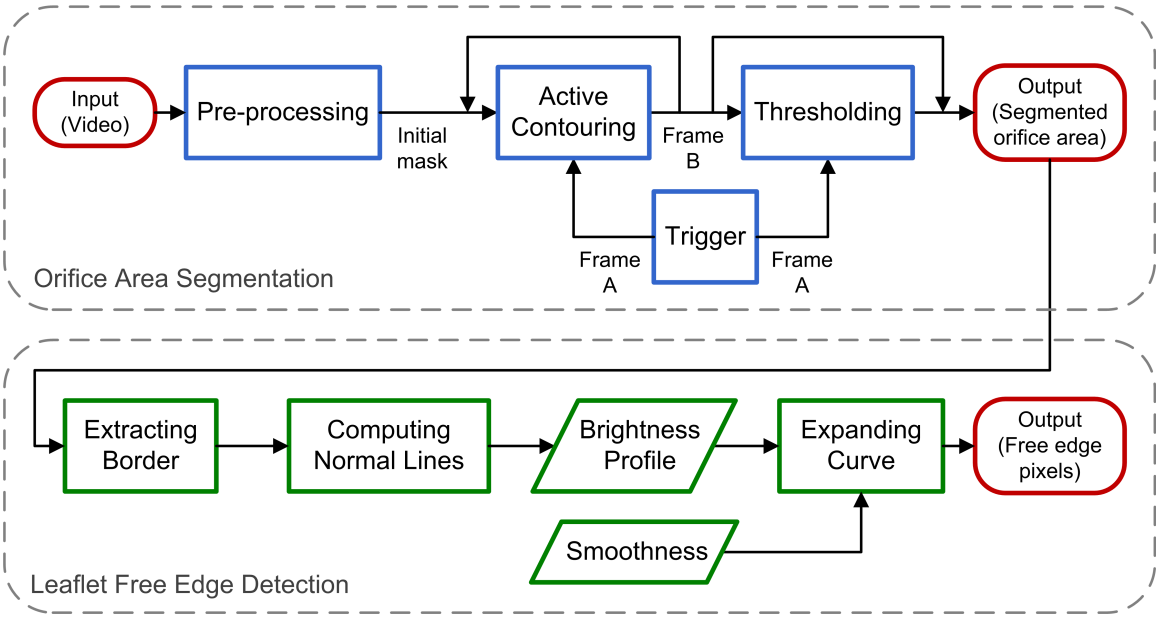


Figure 3.2: Flow chart of the proposed method.

opening area of the valve is segmented via thresholding, then dilated and thinned to remove any artifacts on the borders of the segmented area (Figure 3.3 c). The linear Hough transform is then applied on the thinned segmented area to find the three centerlines, at approximately 120 degrees from each other (Figure 3.3 d). The parameter values of these methods are selected according to available dataset and could be chosen dynamically and analytically, should different dataset be available. The initial mask (Figure 3.3 e) is generated as the triangle connecting three anchor points (red 'x' marks on the circular outline in (Figure 3.3 d) corresponding to the intersection of the centerlines with the circular outline. The three anchor points are found by extending the lines from their end point that is the closest to the circular outline.

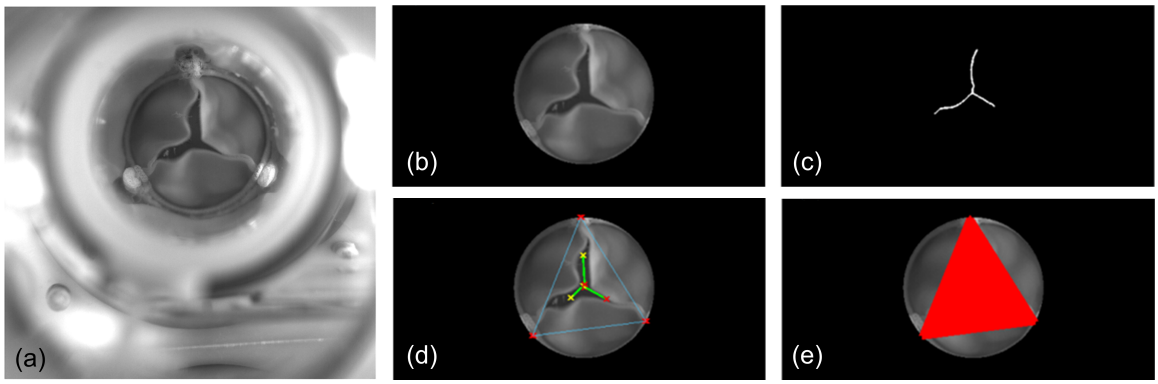


Figure 3.3: Pre-processing: (a) original image, (b) circular outline of the valve (ROI), (c) thinned opening area, (d) centerlines (in green) and corresponding anchor points (in red, on circular outline), and (e) triangular initial mask $M_0$ for active contouring.

### 3.1.2 Trigger

The trigger part determines when to activate (and deactivate) the active contour algorithm, i.e. when the valve is open enough for the active contour to work properly. The maximal circle that can be fitted inside the triangular mask ($MaxC$) is used for observing the gray values of the opening area. Figure 3.4 depicts how the opening area is observed at different frames in the opening phase of the valve. When the mean gray level value decreases by more than 10 % (Eq. 3.1), the corresponding frame (Frame A) is marked as the first one to be segmented via active contouring:

$$|\bar{u_0}(MaxC)_{FrameA} - \bar{u_0}(MaxC)_{FrameA-1}| > 0.1\bar{u_0}(MaxC)_{FrameA-1} \tag{3.1}$$

where $u_0$ is the frame image and $\bar{u_0}(MaxC)_{FrameA}$ is the mean intensity of $MaxC$ in Frame A. The mean intensity of the orifice area in Frame A is used as a threshold for deactivating active contouring at Frame B during the closing phase.

### 3.1.3 Active Contouring

An active contour is a parametric curve. The segmentation is carried out as a minimization of the energy of this spline, which is defined as a combination of internal and external energy terms. The external energy coming from the image data pushes the active contour to fit the data (here the boundaries of the visible orifice area), while the internal energy restricts its deformation to ensure its smoothness. We used the Chan-Vese active contour model [19], which tries to separate the image into regions based on intensities as opposed to edges, according to the following energy functional for curve $C$ (Eq. 3.2) and minimization problem (Eq. 3.3):

$$\begin{aligned} F(c_1, c_2, C) &= \mu L(C) + \nu A(in(C)) \\ &+ \lambda_1 \int_{in(C)} |u_0(x,y) - c_1|^2 dxdy \\ &+ \lambda_2 \int_{out(C)} |u_0(x,y) - c_2|^2 dxdy \end{aligned} \tag{3.2}$$

$$\inf_{c_1, c_2, C} F(c_1, c_2, C) \tag{3.3}$$

where $u_0$ is the frame image, $c_1$ and $c_2$ are respectively the averages inside ($in$) and outside ($out$) $C$, $L$ and $A$ represent the length and area, respectively, and $\mu \geq 0$, $\nu \geq 0$, $\lambda_1 > 0$, and $\lambda_2 > 0$ are fixed parameters typically $\lambda_1 = \lambda_2 = 1$, $\nu = 0$, and $\mu$ is selected according to the specific data corpus. In our case $\mu = 1$ provided the accurate results for the available dataset. Should more videos recorded under variable conditions be available, one could set an automatic calibration process for tuning these parameters to better suit more general conditions.

At Frame A, the active contour is initialized using the contour of the initial triangular mask. The final contour in a given frame, evolved until equilibrium, is used as the initial approximation for the next frame. This procedure continues until the

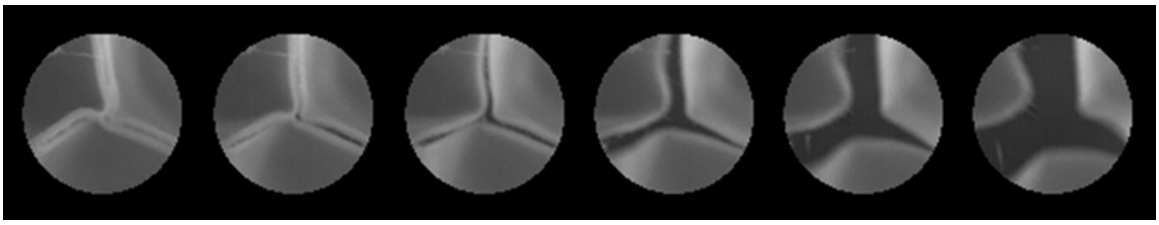

Figure 3.4: Triggering active contouring: observation of the mean gray level value inside the maximal circle fitted inside the initial triangular mask, at different frames of the opening phase. The last circle on the right corresponds to Frame A.

valve is almost closed (Frame B). The segmented orifice areas ($OA$) at each frame are obtained from the pixels located inside the evolved curve $C$. They may be smaller than the actual orifice areas due to the positioning of the leaflets (Figure 3.1), and will be enlarged via the leaflet free edge detection algorithm.

### 3.1.4 Thresholding

For the few frames before the valve is open enough for active contouring (before Frame A) and for those after the valve is almost closed (after Frame B), global thresholding (here, 0.2 over a maximal value of 1 is chosen empirically) is used to segment the orifice area.

## 3.2 Leaflet Free Edge Detection

The proposed leaflet free edge detection algorithm is summarized in Figure 3.2 (bottom). The goal is to detect the free edges of the leaflets in every frame in the valve cycle, by extending the curve derived from the segmented orifice area (section 3.1) that could have stopped short of the actual free edges, thus addressing the issue of the inner side of the leaflets bordering the orifice area. Starting from the border pixels of the segmented orifice area, the curve is expanded along normal lines using a combination of brightness and smoothness criteria, yielding the set of free edge pixels

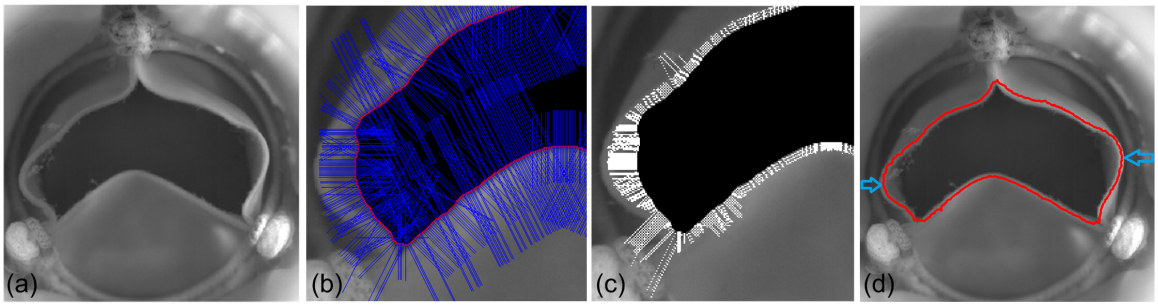


Figure 3.5: Leaflet free edge detection: (a) cropped region of initial frame, (b) normal lines (blue) to each segmented orifice border pixels (red) and segmented orifice area (black), (c) expanded normal lines showing a jagged profile (white) when considering only the brightness criterion, and (d) detected free edge pixels (red) when considering both brightness and smoothness criteria. Blue arrows in (d) point to key expansion locations; the actual free edges were successfully recovered.

as output. Figure 3.5 illustrates the various steps.

### 3.2.1 Extracting Border

The boundary pixels of the segmented orifice area $OA$, obtained from the output of the first algorithm, are first extracted to form the initial free edge border:

$$FE = \{(x, y) \in u_0 \mid B_{OA}(x, y) = 1\} \tag{3.4}$$

where $B$ indicates the boundary. The segmented orifice areas are also superimposed on the original frames to change the corresponding pixel intensities to 0 (black) (Figure 3.5 b).

### 3.2.2 Computing Normal Lines

The next step is to compute a normal line to each border pixel. We find the orientation of the normal line at each border pixel $fe_i \in FE$ via the first derivative in the $X$ and $Y$ directions:

$$N_{orientation}(fe_i) = -dx/dy \tag{3.5}$$

We then extend the normal lines locally from the border pixels inward and outward of $OA$, by 25 pixels (Figure 3.5 b, blue lines), thus obtaining two sets of pixels $NFE_{in}$ and $NFE_{out}$ for each border pixel $fe_i$. The length of the normal lines could also be determined dynamically as a percentage of the valve's radius.

### 3.2.3 Brightness Profile

Free edge pixels tend to have the brightest intensity value locally. We thus compute the intensity profile along each normal line, find the maximal value in the profile, then expand the orifice by incorporating the normal line going from the border pixel to the location of the maximum (Figure 3.5 c):

$$\begin{aligned} EOA_{MaxB} = OA \ \cup \ \{nfe_1, ..., nfe_{max} \mid u_0(max) \\ = \max_{j \in NFE_{in}, k \in NFE_{out}} (u_0(j), u_0(k))\} \end{aligned} \tag{3.6}$$

where $nfe_1$ is the border pixel (first element of $NFE_{in}$ and $NFE_{out}$ for $fe_i$) and $nfe_{max}$ corresponds to the pixel with maximal value in either $NFE_{in}$ or $NFE_{out}$. Morphological closing is then applied on the new extended orifice area $EOA_{MaxB}$ to fill any gap between the added normal lines. A first set of free edge pixels $FE_{MaxB}$ is derived from the boundaries of $EOA$:

$$FE_{MaxB} = \{(x, y) \in u_0 \mid B_{EOA_{MaxB}}(x, y) = 1\} \tag{3.7}$$

where B denotes the boundary.

### 3.2.4 Smoothness

In some regions, especially close to the commission points of the valve leaflets, the pixel with the maximal brightness may not correspond to a free edge pixel, and may consequently cause a false detection (Figure 3.5 c, lower left region). To overcome this issue, the smoothness of the final contour obtained from the extended orifice area is also considered. A second set of free edge pixels $FE_{LocB}$ is found by selecting the local (instead of absolute) maximal brightness pixels in the normal line profiles that are closer to the segmented orifice area:

$$\begin{aligned} EOA_{LocB} &= OA \cup \\ &\{nfe_1, ..., nfe_{max} \mid u_0(max) = peak, \\ &\quad dist(max, 1) = \min_{j \in Peaks}(dist(j, 1))\} \end{aligned} \tag{3.8}$$

$$FE_{LocB} = \{(x, y) \in u_0 \mid B_{EOA_{LocB}}(x, y) = 1\} \tag{3.9}$$

where $Peaks$ represents the set of pixels along the normal lines $NFE_{in}$ and $NFE_{out}$ for which the intensity corresponds to a $peak$ value.

### 3.2.5 Expanding Curve

For each original border pixel, the two sets $FE_{MaxB}$ and $FE_{LocB}$ are compared. The corresponding pixel in either $FE_{MaxB}$ or $FE_{LocB}$ providing the smoother final contour (i.e. the smallest distance with the neighboring border pixel) is selected as the final free edge pixel:

$$\begin{aligned} FE_{Final} = \big\{ &\{fe_{i+1} \in FE_{MaxB} \mid dist(fe_{i+1}, fef_i) < dist(fe_{j+1}, fef_i)\} \cup \\ &\{fe_{j+1} \in FE_{LocB} \mid dist(fe_{j+1}, fef_i) < dist(fe_{i+1}, fef_i)\}\big\} \end{aligned} \tag{3.10}$$

where $fef_i$ is already in $FE_{Final}$. The final expanded curve that represents the leaflet free edges is the collection of all final candidate free edge pixels (Figure 3.5 d).

## 3.3 Experimental Results

### 3.3.1 Experimental Setup and Video Dataset

Our experimental setup is based on the tricuspid biological PHVs, submitted to mechanical simulations using the Pulse Duplicator system from ViVitro Labs Inc., which is the world's most widely cited and most used *in vitro* cardiovascular hydrodynamic testing system [41]. The Pulse Duplicator simulates one half of the human heart and generates a pulsatile flow through the mounted PHV. Flow and pressure sensors, located on each side of the valve, measure and collect the flow data during each simulation.

Videos of the simulations are acquired using a Photron SA3 high speed digital camera in .avi format with a frame rate of 1000 fps, a 1/1000 s shutter speed, and a test cycle of 300 frames, i.e. from the moment the valve opens until it closes completely, with resolutions between 400x400 and 1024x1024 pixels depending on the valve. The dataset used in the experiments comprises three videos of a complete heart beat cycle, taken from 3 different PHVs, for a total of 1745 frames.

Ground truth (GT) data are obtained in a semi-automatic fashion via a combination of automated processing and user input to generate a high-quality three-level image, with the three values denoting the central orifice area, the edge of the orifice that is occluded by the leaflets (inner leaflet area), and the background (other). Figure 3.6 shows sample GT three-level images. To obtain the actual orifice areas (inside the free edges of the leaflets) and utilize the GT data for algorithmic evaluation, central orifice and inner leaflet regions are merged and considered as a single

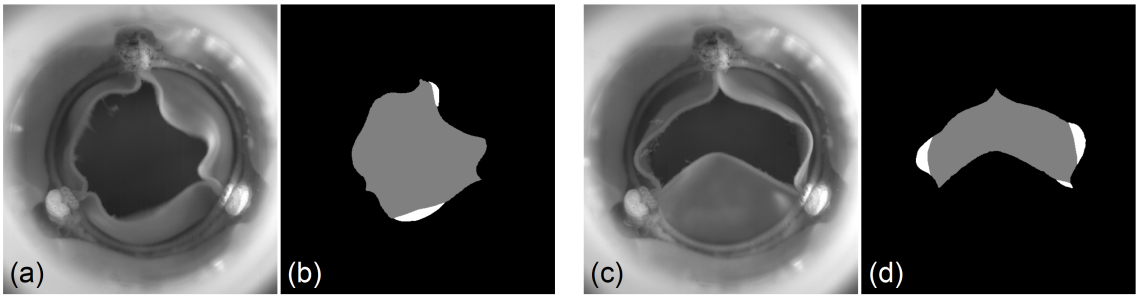


Figure 3.6: Sample GT three-level images. (a) and (c) cropped region of original frames and (b) and (d) corresponding GT data. Gray=central orifice area, white=inner leaflet areas, black=other.

entity.

### 3.3.2 Experimental Evaluation

The proposed extension scheme for the detection of the leaflet free edges (section 3.2) is compared to the active contour-based orifice area segmentation (section 3.1, based on the work in [27]), the latter acting as a baseline. First the PHVs' orifice curves are compared, which constitute key data for PHV performance evaluation. Figure 3.7 illustrates the orifice area over time for the three PHVs. For the proposed method, the orifice area is computed from the region bordered by $FE_{Final}$. The results are in very good agreement with the ground truth, both in terms of trend and magnitude, and show a significant improvement over the baseline, which systematically falls short of the actual orifice area. Table 3.1, which shows the RMSE (root-mean-square error) values for the three valves computed from the differences with the ground truth, confirms the accuracy of the proposed method versus that of the baseline. The information extracted from the proposed method can be used, for instance, to determine how fast the valve opens and closes, how long its stays open, as well as its maximum opening, which constitute crucial data for PHV design assessment.

Although the orifice curves are relevant from a valve evaluation perspective, they

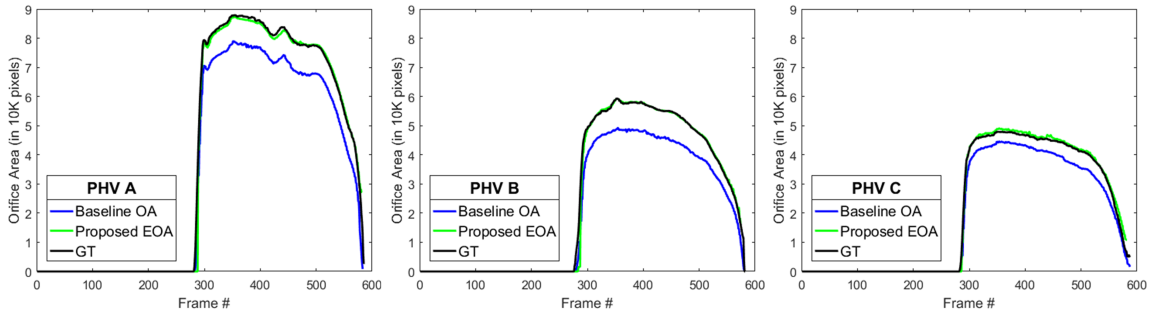


Figure 3.7: Comparison of the segmented orifice areas over time for the baseline and proposed approaches with the ground truth data (GT).

Table 3.1: RMSE values of the segmented orifice areas for the baseline and proposed approaches, both absolute (in pixels) and relative (to the maximal orifice area).

| Method | PHV A | PHV B | PHV C |
|---|---|---|---|
| Baseline OA | 6996 (8.0%) | 6242 (10.5%) | 3215 (6.7%) |
| Proposed EOA | 2409 (2.7%) | 1898 (3.2%) | 972 (2.0%) |

do not allow to properly evaluate the orifice shape accuracy. Therefore, the proposed approach is also evaluated by a boundary matching metric, i.e. the Hausdorff distance, defined between curves $A$ and $B$ as follows [18]:

$$d_H(A,B) = \max\left(\max_i\{d(a_i,B)\}, \max_j\{d(b_j,A)\}\right) \tag{3.11}$$

$$d(a_i,B) = \min_j \|b_j - a_i\| \tag{3.12}$$

where $a_i$ is a point on $A$ and $b_j$ a point on $B$. Table 3.2 shows the average $d_H$ over all frames between the ground truth and the orifice boundaries extracted by the baseline and the proposed approaches, for the three PHVs. The smaller distances obtained for the proposed method confirm its ability to recover the shape of the actual orifice area more accurately than the baseline. On a frame-by-frame basis, the largest distances typically occur when the valve is almost closed.

Figure 3.8 shows typical examples of the orifice boundaries extracted by the base-

Table 3.2: Average Hausdorff distance $d_H$ ($\pm$ standard deviation) in pixels between the ground truth and the orifice boundaries for the baseline and proposed approaches.

| Method | PHV A | PHV B | PHV C |
|---|---|---|---|
| Baseline OA | 19.0 $\pm$ 4.3 | 32.8 $\pm$ 9.9 | 14.6 $\pm$ 6.0 |
| Proposed EOA | 8.7 $\pm$ 3.7 | 14.0 $\pm$ 12.2 | 11.5 $\pm$ 6.6 |

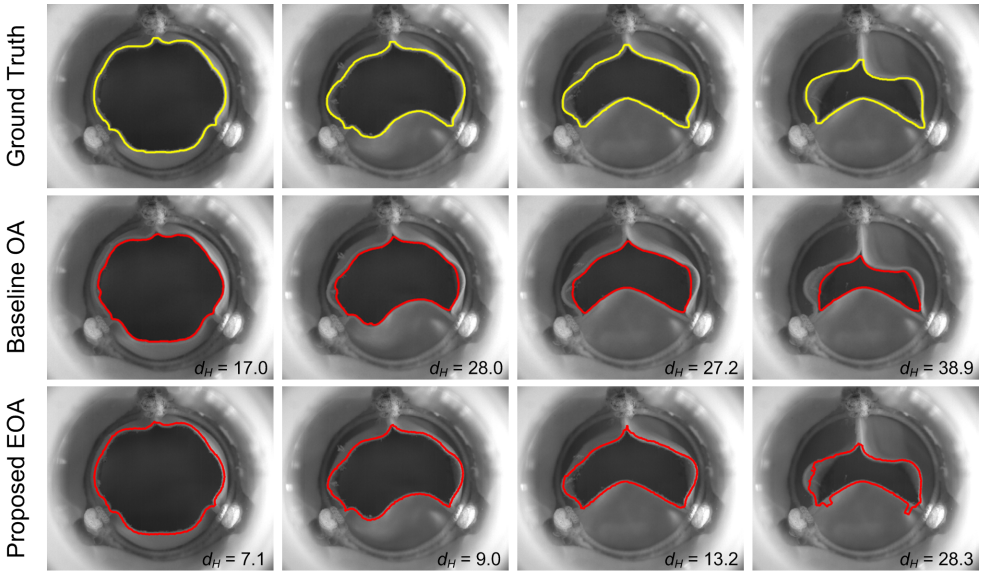


Figure 3.8: Typical results and Hausdorff distances $d_H$, at different moments in the cycle, for the baseline and proposed approaches, along with the ground truth, for PHV A.

line and the proposed approaches at various moments in the cycle, along with $d_H$ values. The first three columns constitute good cases, in which the proposed approach successfully tracked the leaflet free edges, whereas the baseline approach failed locally either due to the leaflet's visible inner side (2nd and 3rd columns), or due to the presence of small attached pieces (see 1st column, left region). The last column constitutes an example where our approach yielded to errors due to local brightness maxima, typically occurring near the commission points. This issue will be addressed by the approach proposed in Chapter 4.

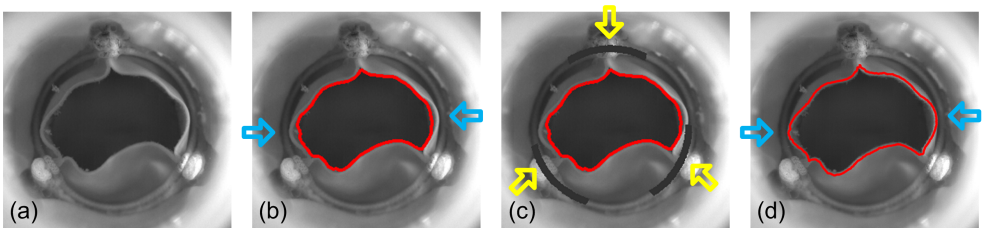


Figure 3.9: Comparison with attractors (yellow arrows): (a) original (cropped) frame, results (red) of [27] (b) without and (c) with attractors and (d) of our proposed method. Blue arrows indicate problematic areas, where attractors fail and our method succeeds.

### 3.3.3 Comparison with Attractors

The proposed free edge detection approach is also compared to that of Condurache et al. [27], which is based on attractors. They proposed adding attractors (i.e. artificial sharp edges) to the circular outline of the valve, on both sides of the commission points, in order to improve the active contour segmentation and detect the actual orifice area. However, this approach works only in cases where the leaflet free edges are located on the circular outline, which only covers a special case of valves and motion. Figure 3.9 shows that their proposed method is unable to successfully detect the leaflet free edges when the valve's motion is such that leaflet inner sides are visible and the edges are away from the circular outline. The sample frame is segmented with and without using the attractors, which yield the same incorrect results. Results obtained with our proposed method are also shown for comparison purposes.

## 3.4 Conclusion

This chapter presented an automatic approach for the quantitative performance analysis of bioprosthetic heart valves from high-speed videos recorded during *in vitro* simulations of the opening and closing motions. The proposed approach addresses the issue of the valve orifice being partially bordered by the inner side of its leaflets,

by tracking the actual leaflet free edges. An initial estimation of the valve orifice area is first obtained via active contouring and then refined via a curve extension scheme based on brightness and smoothness criteria, allowing the method to successfully segment the orifice area for valve design evaluation purposes. Evaluation on videos from three different valves demonstrated the effectiveness of the approach to detect the leaflet free edges and thus obtain the actual orifice area over time during the valve cycle. The proposed approach outperformed a baseline algorithm both in terms of valve design evaluation metrics (accuracy of the temporal orifice curves) and computer vision evaluation metrics (accuracy of the orifice shape). Additional comparisons with a recent method based on attractors also showed the proposed method's ability to better detect leaflet free edges.

# Chapter 4

# Improving Robustness and Temporal Accuracy for Leaflet Free Edge Detection

This chapter proposes several modifications and refinements to make the initially developed segmentation approach of Chapter 3, more autonomous, robust, and accurate. As it was highlighted in Chapter 3, some adjustments are needed to improve the performance and increase the reliability of the initial algorithms (Section 4.1). One of the most important challenges was that the free edge detection algorithm was not always able to properly determine the free edge pixels in areas close to the anchor points or when the orifice area has a very narrow arm-like shape and non-homogeneous background, causing disruption in the performance of active contours. To overcome this issue, it is proposed to combine the strength of both thresholding and active contouring, as opposed to utilizing active contouring only. This improves results particularly in elongated areas of the valve orifice and allows for correctly processing more frames when the valve is almost closed (Section 4.1.1). In addition, in

the contour transformation mechanism, it is proposed to utilize orthonormal curves instead of lines, which allows us to better cope with problematic frames that have local brightness maxima occurring near the commission points of the valve. Orthonormal curves are also more adequate in the general context of non-linear deformable movement analysis (Section 4.1.2). These two proposed modifications cooperate toward yielding to more accurate segmentation of the orifice area and detection of the leaflet borders especially in problematic frames, and make the algorithm more robust and reliable.

The other shortcoming was the necessity to have high frame rate videos as the videos with lower frame rates (less than 1000 fps) would result in blurry edges because of the fast motion of leaflets. A new approach to determine the initial mask in a frame is proposed to address this issue. This method is more robust to the presence of blurry edges (Section 4.1.1). The greater ability to cope with blurry edges is demonstrated via additional experiments on videos with various frame rates (Section 4.2.5). The automatic determination of the opening phase of the valve is also suggested. This feature increases the number of accurately processed frames in opening and closing phases and consequently increases the temporal accuracy of the determined orifice curve.

In section 4.2 the results of the developed algorithms along with the proposed modifications are presented and the accuracy of the segmented orifice area and contour of the free edge of leaflets is investigated by comparing them with those of the baseline method, the initial algorithm, and the ground truth. The comparison confirms the positive effect of proposed modifications on the robustness, reliability, and accuracy of the algorithms' outcomes.

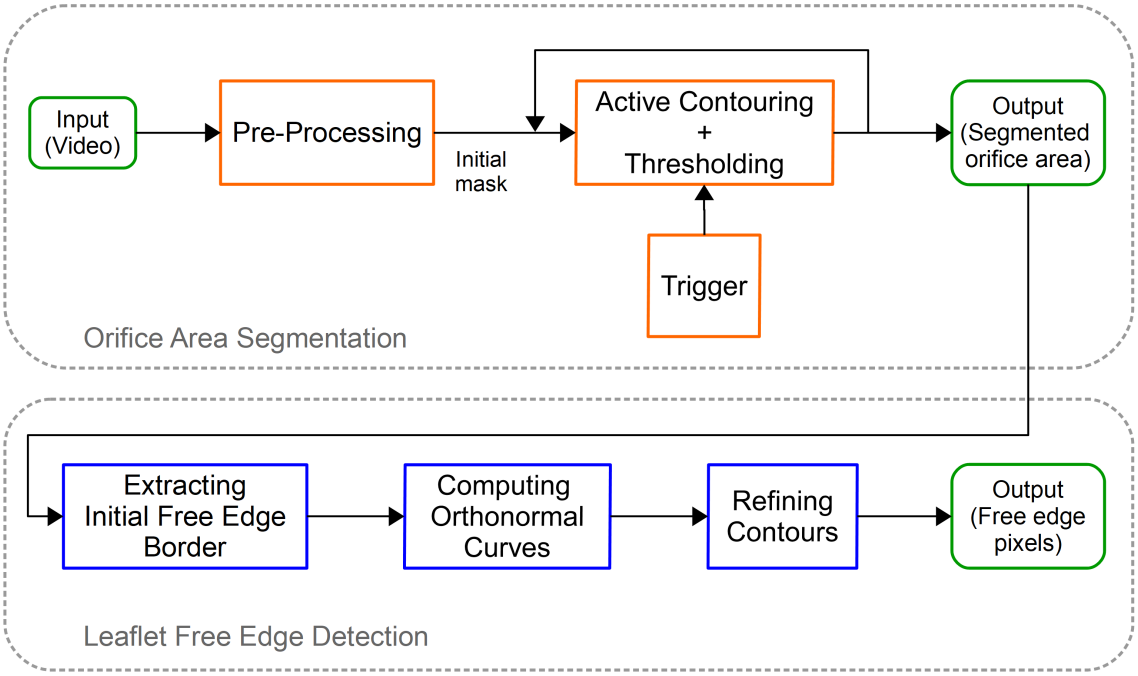


Figure 4.1: Flow chart of the proposed method along with the modifications.

## 4.1 Proposed Modifications

Figure 4.1 shows the flowchart of the developed algorithms along with the proposed refinements. Same as in Chapter 3, there are two interconnected algorithms to extract information from the PHV testing videos that are used for the quantitative assessment of PHV designs: orifice area segmentation and leaflet free edge detection. Three modifications in *orifice area segmentation* and one modification in *leaflet free edge detection* are proposed, as explained in the following sections.

### 4.1.1 Orifice Area Segmentation

One of the weaknesses of the original orifice area segmentation algorithm is that it requires high-quality high frame rate videos to perform properly and provide reliable results. Lower frame rate videos lead to blurry edges in leaflet borders and the current pre-processing step for generating the initial mask requires sharp edges to detect the

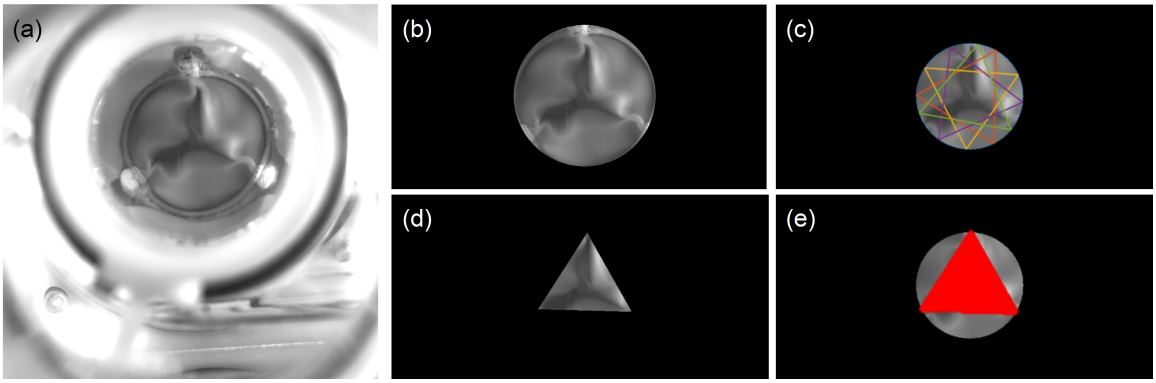


Figure 4.2: Pre-processing: (a) original image, (b) circular outline of the valve (ROI), (c) various potential triangular masks, (d) triangle with lowest average gray value, and (e) final triangular initial mask $M_0$ for active contouring.

opening of the valve and perform several morphological operations for determining the anchor point locations. To overcome this issue, a more robust approach that is not reliant on sharp edges is needed.

Considering that the orifice area is generally darker than the surrounding area and the leaflets' surfaces, the triangle that best encloses the orifice area will have the lowest average gray value. A frame showing a small valve opening (akin to a three-pointed star shape) is preferred for this purpose. The idea **of the first proposed adjustment** is to generate equilateral triangles by connecting each border point on the valve's circular outline to two equally spaced points on the border (Figure 4.2 c). The average gray value of the pixels inside each triangle is calculated and the triangle with the lowest average gray value (Figure 4.2 d) will be selected as the initial mask for active contouring (Figure 4.2 e).

This manner of computing the initial mask is robust to image blurriness caused by a low frame rate, low quality of the videos, and/or the fast movement of the leaflets in the opening stage, as we are not relying on image edges to find the first contour but on average pixel values and general shape considerations.

**The second proposed adjustment** to the pre-processing step is to automati-

cally determine the beginning of the valve opening phase. This new feature in combination with the trigger mechanism yields to better segmentation of more frames in a cycle and it proves to be effective especially in the opening and closing phases. For automatic detection of the valve opening phase, gray level values over the whole cycle are observed (Figure 4.3). When the valve starts to open, its leaflets move toward the light source and become brighter; there is thus a sudden increase in gray-level value (Figure 4.3, Region 1). On the other hand, as the orifice area is darker than the surrounding areas (including the leaflets), the following frames are characterized by a sudden drop in the average gray-level value (Figure 4.3, Region 2). The start of the opening phase is found as the frame (Frame 0) corresponding to the steep transition between Region 1 and Region 2.

Now that the start of the opening phase (Frame 0) is determined, the change in gray level values of its following frames is analyzed in order to determine when the valve is open enough for active contouring (as described in Section 3.1).

**The third proposed modification** is related to the segmentation of the orifice area. Analyzing the outcome of the original orifice area segmentation showed that for some of the frames, especially in the opening and closing phases where the valve is not completely open, active contouring has difficulties segmenting the orifice area accurately. In narrow arm-shaped and small pointy areas close to commission points, the deformable contour has issues reaching the borders of the opening area due to its internal energy terms (See Figure 4.4). Since these narrow areas are small and generally homogeneously dark, it is proposed to also use global thresholding to compensate for this deficiency and combine the results of both active contouring and thresholding to obtain OA. Figure 4.5 a shows how the combination of active contouring and thresholding results can complement each other and provide a more accurate segmented orifice area. White indicates pixels that both methods can segment, ma-

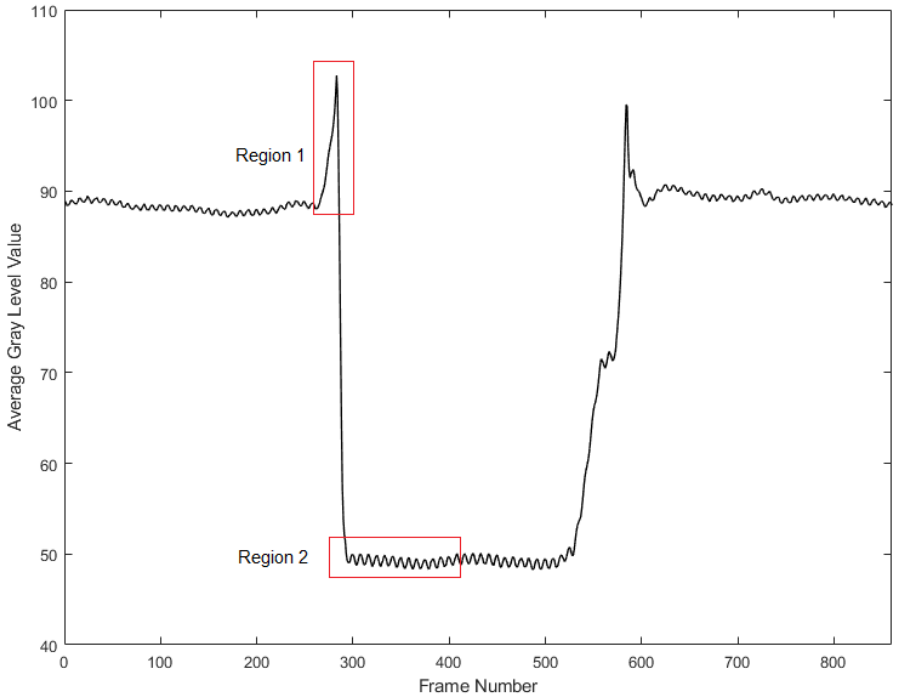


Figure 4.3: The start of the opening phase of the valve is determined from a sudden increase (Region 1) followed by a sudden drop (Region 2) of the average gray level value of the frame.

genta indicates pixels segmented by active contouring only, and green indicates pixels segmented by thresholding only. Many pixels from the narrowing arm region at the bottom left are missed by active contouring (green).

One may note that thresholding cannot be used reliably as the sole approach for segmenting the orifice area because of the non-homogenous regions, as shown in Figure 4.5 c, as many pixels are missed by thresholding (magenta), especially toward the orifice borders. Figure 4.5 b and d show the borders of the segmented areas (combined thresholding and active contouring of Figure 4.5 a and c, respectively) as red contours superimposed on the original images. In both cases, the red borders are short of the actual orifice borders, justifying the need for the proposed leaflet free edge detection algorithm (Section 3.2). A threshold of 0.2 over a maximal value of 1 typically provides acceptable results.

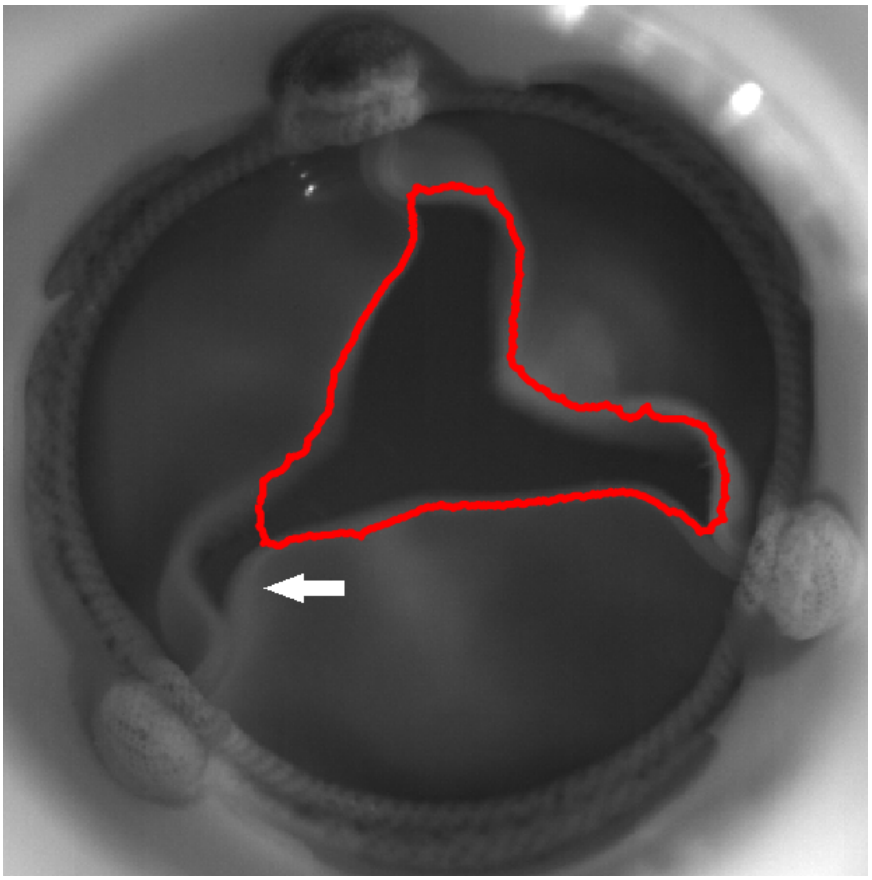

Figure 4.4: Example frame with narrow arm-shaped and pointy area close to comission points; white arrow points to the problematic area where active contouring could not successfully reach the border of the orifice area.

### 4.1.2 Leaflet Free Edge Detection

Figure 4.1 (bottom) presents an overview of the leaflet detection algorithm with the proposed refinements. This algorithm aims to address the issue of the visible inner side of the leaflets bordering the orifice area. The idea is to detect the free edges of the leaflets in every frame of the valve cycle by refining the contour derived from the segmented orifice area $OA$ (Section 3.1), that could have stopped short of the actual free edges. Starting from the boundary pixels of $OA$, we propose to modify the contour along orthonormal curves rather than the normal lines used in the initial leaflet free edge detection algorithm. The combination of the extended contour and

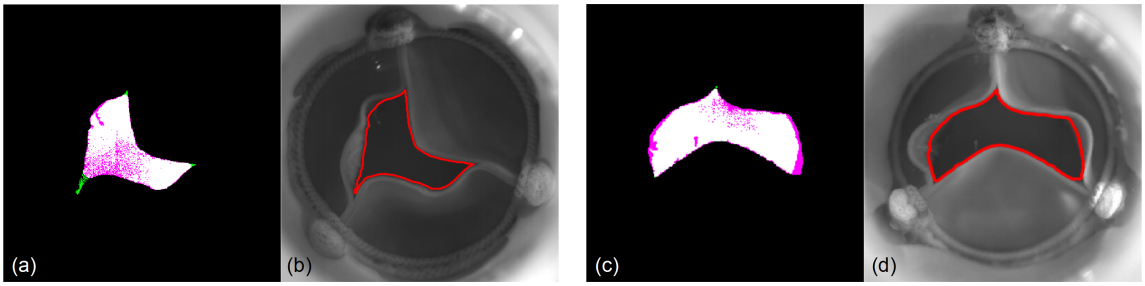


Figure 4.5: Combining active contouring and thresholding. (a,c) Segmented orifice area pixels for two different cases, with white indicating pixels segmented by both methods, magenta indicating pixels segmented by active contouring only, and green indicating pixels segmented by thresholding only. (b,d) The corresponding borders of the combined segmented pixels are shown in red, superimposed over the original frames.

the brightness and smoothness criteria will result in the set of free edge pixels as output. More details of the proposed modifications are as follows.

The initial free edge border (FE) is created by the boundary pixels of $OA$ (Eq. 3.4), output of the first algorithm (Figure 4.6 c, red). The next step is to compute an orthonormal curve to each boundary pixel. The orthonormal curves serve as potential refinement directions, allowing us to reach the actual free edges. A second-degree polynomial is fitted to each pixel $fe_i \in FE$ with coordinates $(x, y)$ and its 5-pixel neighborhood (Figure 4.6 b, green curves):

$$y = ax^2 + bx + c \tag{4.1}$$

where $a$, $b$, and $c$ are constants derived from the fitting process (least-square error). The orthonormal curve to the short fitted curve in above equation (Figure 4.6 b, blue curves) can then be calculated using:

$$y = \frac{-1}{2a} \ln |2ax + b| + c' \tag{4.2}$$

where $c'$ is a constant. A set of pixels $NFE$ along the orthonormal curve is obtained

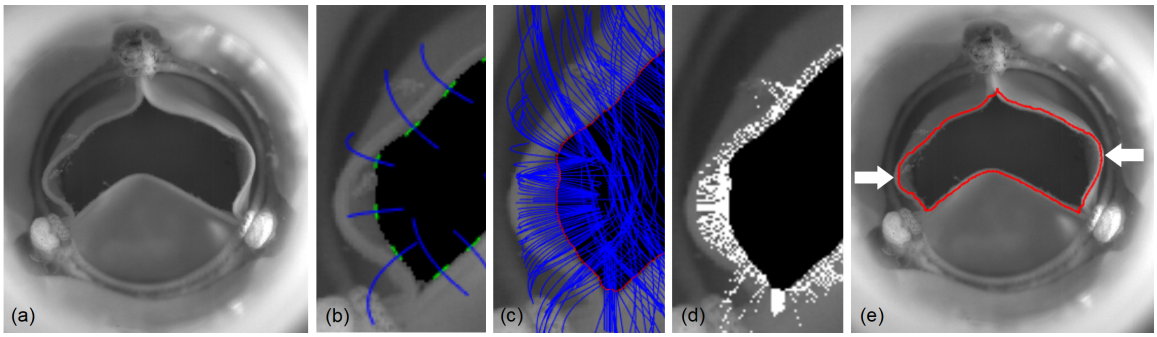


Figure 4.6: Leaflet free edge detection: cropped region of initial frame (a), examples of short fitted curves along boundary pixels (green), corresponding orthonormal curves (blue), and segmented orifice area (black) (b), full orthonormal curves (blue) (c), modified orifice area along orthonormal curves (white) when considering only the absolute maximal brightness (d), and detected free edge pixels (red) when considering also the local maximal brightness and smoothness of the contour (e). White arrows in (e) point to key refinement locations; the actual free edges were successfully recovered.

for each boundary pixel $fe_i$. Figure 4.6 c shows the full orthonormal curves (blue) to the pixels in $FE$ (red), that constitute potential modifications to the contour.

The orthonormal curves are chosen over normal lines for two reasons. First, the curves are more suited to the context of non-linear movement/deformation undergone by the valve leaflets. Second, the curves allow us to better cope with problematic frames, especially when there is a local brightness maximum near the commission points (e.g. Figure 4.6 a, the two lower commission points). Since the proposed transformation mechanism relies in part on brightness (see Section 3.2.3), orthonormal curves, compared to normal lines, are less likely to converge falsely toward the commission points due to their curved shape; those that do will be in lesser numbers and as such dismissed as outliers when considering the smoothness of the contour (see Section 3.2.4). Figure 4.7 shows the difference between the use of normal lines and that of orthonormal curves in the false inclusion of commission points as part of the leaflet free edges. The candidate free edge pixels are then selected considering both brightness and smoothness criteria (see Section 3.2.5).

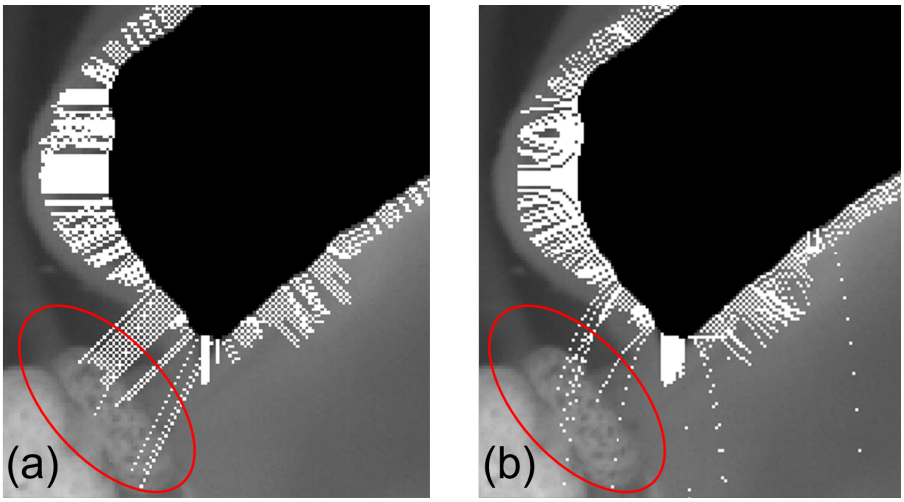


Figure 4.7: Refining the orifice area along normal lines (a) vs. orthonormal curves (b). The regions inside the red ellipses show less candidate pixels for contour refinement when using orthonormal curves in the case of bright commission points in the vicinity of the boundary pixels.

### 4.1.3 Experimental Setup and Video Dataset

In the absence of public PHV video datasets, a video dataset based on an experimental setup with aortic biological PHVs submitted to the Pulse Duplicator system from ViVitro Labs Inc. is assembled. As it was mentioned in the Chapter 3 (see Section 3.3.1), the Pulse Duplicator simulates one half of the human heart and generates a pulsatile flow through the mounted PHV. Videos of the simulations are recorded for three different PHVs via a Photron SA3 highspeed digital camera using the settings presented in Table 4.1. Sample frames are shown in Figure 1.4.

The dataset comprises five videos for a total of 3212 frames, with 1142 showing the valves either partially or completely open (i.e., segmentable frames). The videos are split into two subsets:

- high quality (PHVs A, B, and C at 1000 fps: PHV A, PHV B, and PHV C),
- variable quality (PHV A at 1000, 500, and 250 fps: PHV A @1000, PHV A @500, and PHV A @250).

The first subset is used in the main experiments (Section 4.2), and the second one is an experiment on the impact of the frame rate (Section 4.2.5).

Table 4.1: Video settings.

| Value | PHV A | | | PHV B | PHV C |
|---|---|---|---|---|---|
| Shutter speed (s) | 1/1000 | 1/500 | 1/250 | 1/1000 | 1/1000 |
| Test cycle* (frames) | 857 | 430 | 215 | 857 | 857 |
| Resolution (pixels) | 1024x1024 | 1024x1024 | 1024x1024 | 400x400 | 400x400 |
| Frame rate (fps) | 1000 | 500 | 250 | 1000 | 1000 |

*A test cycle covers the opening phase, the open phase, the closing phase, and the closed phase, until the valve begins a new opening phase.

## 4.2 Experimental Results

Here, the proposed modified approach is compared with the initial algorithm (described in Chapter 3) as well as the active contour-based orifice area segmentation ($OAS$) [27], as the reference method, on a dataset assembled from a data on three different PHVs. These methods of comparison are referred as OAS and Orthonormal Line-based Free Edge Detection (OLFED) respectively. The proposed method is also referred as Automatic Orthonormal Curve-based Free Edge Detection (AOCFED).

### 4.2.1 Valve design-related metrics

The first feature to compare is the orifice area curve, which is key data for PHV performance evaluation. Figure 4.8 shows the evolution of orifice area over time for the three PHVs (videos PHVA , PHV B, and PHV C). For the proposed method (AOCFED), the orifice area is computed from the region bordered by $FE_{Final}$. The results are in very good agreement with the GT, both in terms of curve shape and

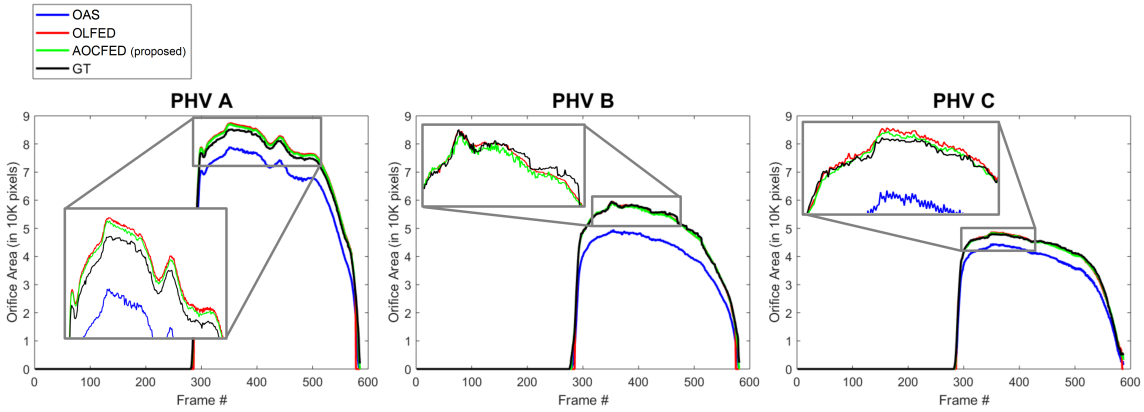


Figure 4.8: Comparison of the extracted orifice areas over time for OAS, OLFED, and AOCFED (proposed) with the ground truth data (GT).

area. They also show a significant improvement over the reference method (OAS), which systematically falls short of the actual orifice area, and a small improvement over the original algorithm for PHVs A and C (OLFED), cases for which the initial algorithm tends to slightly overestimate the actual orifice area. The proposed method also shows an improvement over the original algorithm for PHV B at the beginning of the opening phase (around frame 282). Table 4.2 shows the root-mean-square error (RMSE) values, in terms of extracted orifice areas, for the three PHVs (videos PHV A, PHV B, and PHV C) computed from the differences with the GT. The proposed method outperforms both methods of comparison, having the lowest error for all three PHVs. This is due in part to the more accurate free edge detection, but also to the proposed trigger mechanism and precise determination of the beginning of the opening phase (Frame 0). These two factors enable our algorithm to correctly process more frames in the test cycle, especially the first few frames of the opening phase and the last few frames of the closing phase. The orifice areas extracted from the proposed method can be used to determine how fast the valve opens and closes, how long it stays open, as well as its maximum opening, which constitute crucial data for PHV design assessment.

Table 4.2: RMSE values of the extracted orifice areas for OAS, OLFED, and AOCFED (proposed), both absolute (in pixels) and relative (to the maximal orifice area).

| Method | PHV A | PHV B | PHV C |
|---|---|---|---|
| OAS | 5096 (6.0%) | 6329 (10.6%) | 3179 (6.6%) |
| OLFED | 2544 (3.0%) | 1635 (2.7%) | 647 (1.3%) |
| AOCFED (proposed) | 1035 (1.2%) | 601 (1.0%) | 363 (0.8%) |

### 4.2.2 Computer Vision Related Metrics

The orifice area curves and RMSE are relevant from a valve evaluation viewpoint, nevertheless, they do not allow a proper evaluation of the orifice shape accuracy. Therefore, the proposed method is also assessed using two standard computer vision metrics: the Jaccard similarity coefficient, also known as intersection over union (IoU), and the Hausdorff distance.

The Jaccard similarity coefficient measures the similarity between two sets by comparing the size of the intersection and the size of the union of two sets as:

$$J(P,Q) = \frac{|P \bigcap Q|}{|P \bigcup Q|} \tag{4.3}$$

where $P$ represents the set of pixels detected by an algorithm as being part of the valve orifice, and $Q$ represents the set of pixels actually part of the valve orifice as specified in the GT. The value of $J(P,Q)$ can range from 0 to 1, with 0 indicating no overlap between $P$ and $Q$ and 1 indicating a perfect overlap. Table 4.3 shows the average $J(P,Q)$ over all frames between the GT and the orifice extracted by the proposed approach and the two methods of comparison, for the three PHVs (videos PHV A, PHV B, and PHV C). The proposed method outperforms both methods of comparison, having the highest Jaccard similarity coefficient for all three PHVs.

Table 4.3: Average Jaccard similarity coefficient (IoU) (± standard deviation) between the ground truth and the extracted orifices for OAS, OLFED, and AOCFED (proposed).

| Method | PHV A | PHV B | PHV C |
|---|---|---|---|
| OAS | 0.871 ± 0.143 | 0.789 ± 0.140 | 0.865 ± 0.113 |
| OLFED | 0.927 ± 0.197 | 0.907 ± 0.215 | 0.937 ± 0.149 |
| AOCFED (proposed) | 0.953 ± 0.094 | 0.933 ± 0.119 | 0.956 ± 0.078 |

The similarity values close to 1, ranging from 0.933 to 0.956, confirm the ability of the proposed method to retrieve the valve orifice shape and location accurately.

The Hausdorff distance is a boundary matching metric and is defined between boundaries R and S as described in Eqs. (3.11) and (3.12). Table 4.4 shows the average $d_H$ over all frames between the GT and the orifice boundaries extracted by the proposed approach and the two methods of comparison, for the three PHVs (videos PHVA, PHV B, and PHV C). If a method did not detect an actual opening of the valve in a given frame, which typically happens towards the beginning or the end of the cycle, the extracted boundary is considered to be a single point to be able to compute a (large) Hausdorff distance and penalize the method. If a method incorrectly detected an opening of the valve in a given frame while the valve was actually closed, the GT is considered to be a single point, again to be able to compute a (large) Hausdorff distance and penalize the method.

As the results show, the proposed method significantly outperforms both the reference method (OAS) and the previous work (OLFED) for all valves, especially for PHV B. The smaller distances obtained for our method, ranging from 7.2 to 11.9 pixels, confirm its ability to recover the shape of the actual orifice more accurately than both methods of comparison. To provide a rough estimate on what these Hausdorff distances mean in terms of real-word measurements, the valve diameter is 25 mm,

Table 4.4: Average Hausdorff distance $d_H$ ($\pm$ standard deviation) in pixels between the ground truth and the orifice boundaries for OAS, OLFED, and AOCFED (proposed).

| Method | PHV A | PHV B | PHV C |
|---|---|---|---|
| OAS | 19.0 $\pm$ 14.5 | 33.2 $\pm$ 14.1 | 14.8 $\pm$ 7.6 |
| OLFED | 14.0 $\pm$ 30.4 | 14.0 $\pm$ 23.8 | 11.8 $\pm$ 12.9 |
| AOCFED (proposed) | 9.8 $\pm$ 13.1 | 11.9 $\pm$ 10.8 | 7.2 $\pm$ 6.8 |

which is approximately equivalent to 200 pixels. An accurate conversion between pixel-based and real-world measurements cannot be done at this point because of a lack of calibration of the camera at the time of the video data acquisition. On a frame-by-frame basis, the largest distances typically occur when the valve is almost closed. This is due to the narrow, pointy regions in those frames, which make the frames more prone to erroneous processing. Furthermore, there are some ripples in the leaflet edges due to fluttering during the opening and closing phases that add to the problem and result in increased distances for these few frames.

### 4.2.3 Qualitative Evaluation

Figures 4.9 and 4.10 show typical examples of the orifice boundaries extracted by the reference method (OAS), the original developed algorithm (OLFED), and the proposed approach (AOCFED) at various moments in the cycle, for PHVs A and B, respectively. Sample results for PHV C are not shown due to intellectual property considerations. White arrows indicate problematic areas for the methods of comparison that the proposed method is able to address. Generally, the reference method (OAS) falls short of the actual free edge pixels. This can be explained by the fact that it works based on segmenting the darker region as the potential orifice area. This approach cannot detect the leaflet free edges when the orifice area is occluded by the

visible inner side of the leaflets.

The approach presented in the previous chapter (OLFED) partially addresses this issue; however, as shown in both figures indicated by the white arrows, the boundaries of the detected orifice area sometimes do not reach the actual leaflet free edges or, in some cases, spill over the edges to reach some other bright regions. For example, for frame 286 of PHV B (Figure 4.10, first row), applying the active contour method alone for segmenting the orifice area (as in OAS) is insufficient to reach the boundaries of the orifice area due to the non-homogeneity and narrow arm shape of the region. Those arm-shaped regions yield strong internal energy terms in the active contour formulation, which stop the deformable contour short of the actual orifice area boundaries. In this particular frame (and a few more similar frames), the problem is so extreme that even the expansion of the segmented opening area boundaries (as in OLFED) cannot push the contour to the actual free edge pixels. By combining thresholding and active contouring (as in the proposed method), the orifice area is segmented more accurately, and consequently, the refinement of its boundaries results in a more accurate detection of the leaflet free edges.

Also, because of the use of orthonormal curves, the possibility of reaching other bright regions instead of the leaflet free edges decreases (see Section 4.1.2, Figure 4.7). One can, therefore, use longer transformation curves without worrying about incorrect bright regions. This is especially helpful when a larger region of the inner side of the leaflet is visible (e.g., frame 571 of PHVA, last row of Figure 4.9). In the original developed algorithm (OLFED), the normal lines had to be kept as short as possible to prevent an incorrect detection of the other bright regions such as commission points.

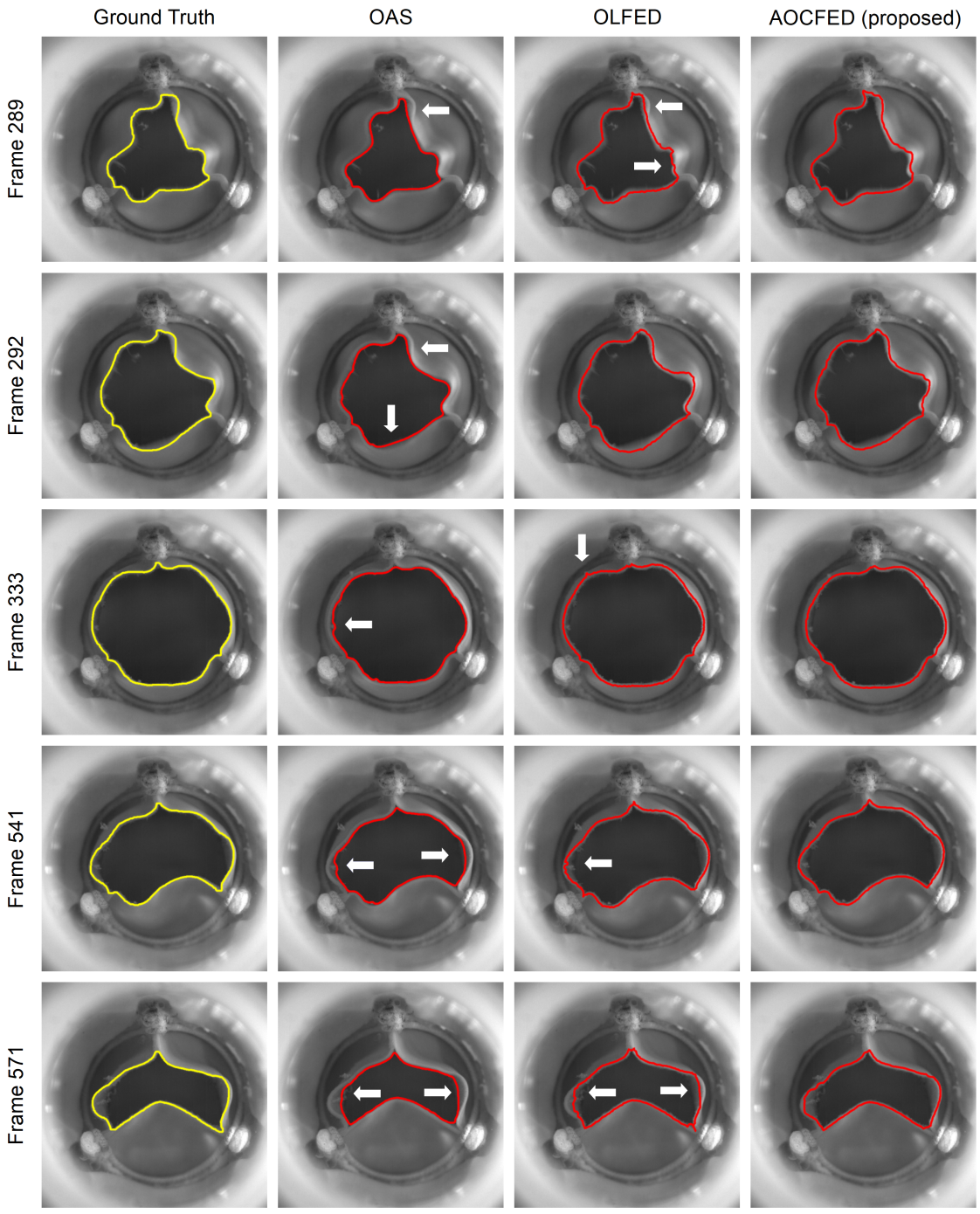


Figure 4.9: Typical results at different moments in the cycle for OAS, OLFED, and AOCFED (proposed), along with the ground truth, for PHV A. Frames are cropped for visualization purposes. White arrows indicate issues that the proposed method is able to successfully address.

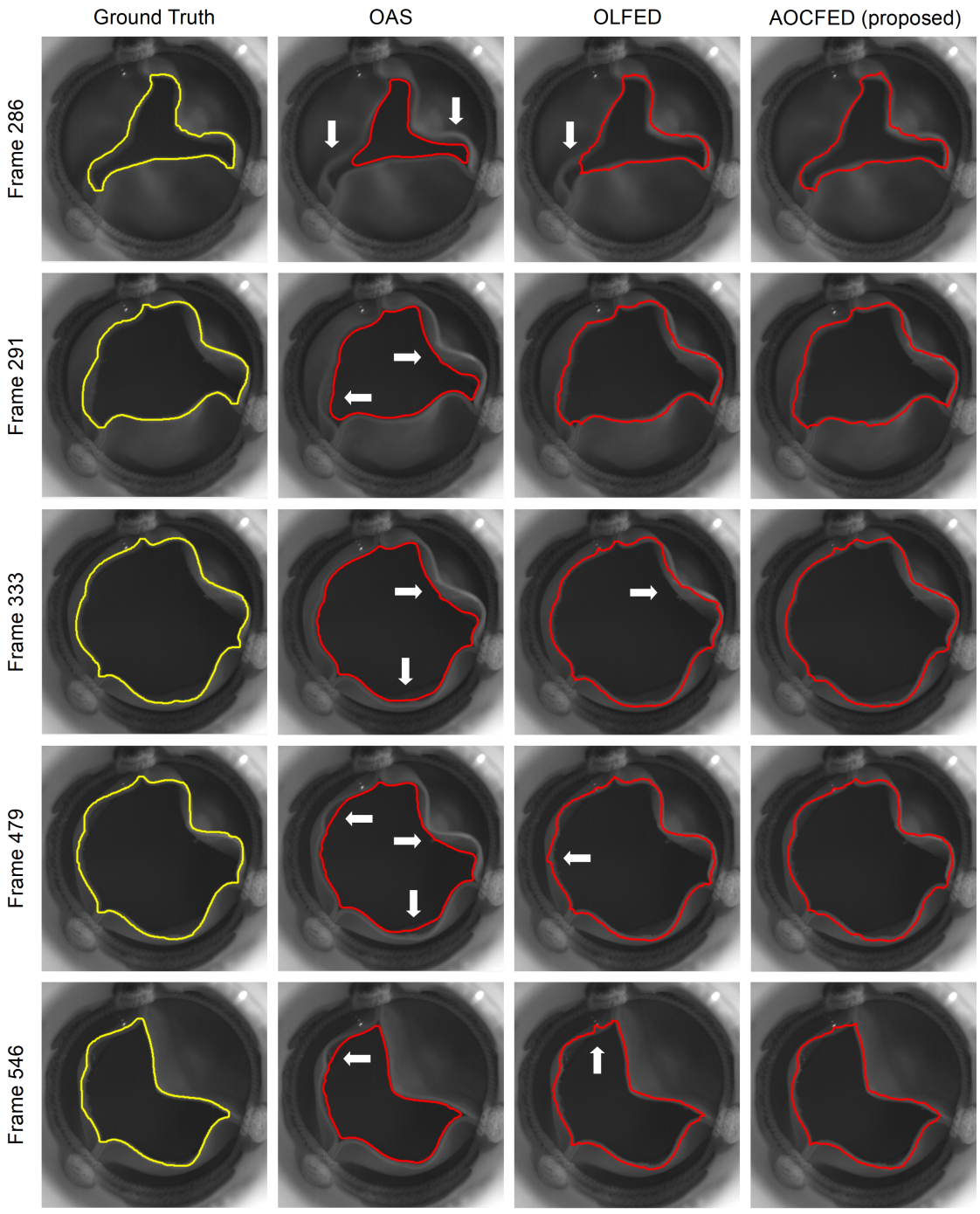


Figure 4.10: Typical results at different moments in the cycle for OAS, OLFED, and AOCFED (proposed), along with the ground truth, for PHV B. Frames are cropped for visualization purposes. White arrows indicate issues that the proposed method is able to successfully address.

### 4.2.4 Other Elements of Discussion

Another feature of the proposed method, which significantly affects the valve design quality metrics (orifice area curves and their RMSE values), relates to the precise determination of the beginning of the opening phase (Frame 0) (see Section 4.1.1). That determination decreases the chances of processing frames outside of the open phase. If an algorithm starts after the actual opening of the valve (and stops before the actual closing of the valve), each missed frame results in a significant error in the performance evaluation metrics. Starting before the actual opening (and stopping after the actual closing of the valve) is equally penalizing. The proposed method performs better in this regard compared to the previous algorithm, (OLFED). For instance, the previous method missed seven frames at the start of the opening phase and eight frames at the end of the closing phase for PHVA. In comparison, the proposed method missed only one frame at the end of the closing phase for the same video. This is a significant improvement, considering that some valve design malfunctions relate to their improper closing; being able to process and correctly segment the orifice area when the valve is almost closed is thus crucial.

The reference method (OAS), which is solely based on active contouring, fails to detect the leaflet free edges whenever the inner side of the leaflets is visible and consequently the border of the segmented orifice area does not match the actual leaflet free edges. This can happen at any time during the cycle, i.e., during the opening phase, the closing phase, and when the valve is open. Also, active contouring alone is not always successful in segmenting the orifice area accurately, especially for frames in the opening and closing phases where the background of the valve orifice is not homogenous.

Although the issue of the visible inner side of the leaflets was addressed in the previously developed algorithm (OLFED), it was still unable to accurately segment

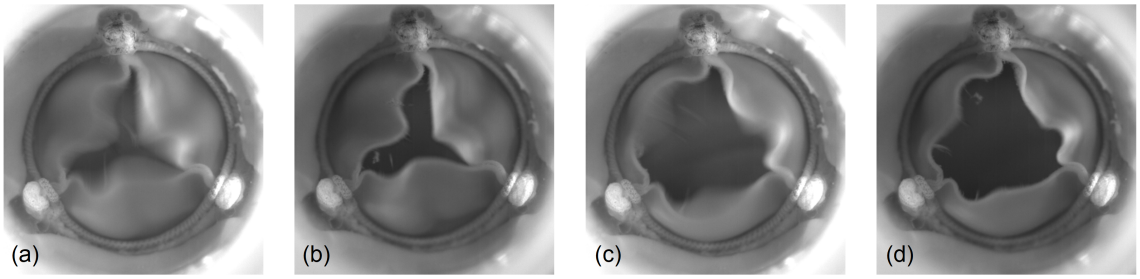


Figure 4.11: Impact of frame rate on image bluriness. (a and c) Sample (cropped) frames at 250 fps and (b and d) corresponding frames at 1000 fps.

the orifice area—and consequently the free edges of the leaflets—for several frames in the opening and closing phases of the cycle. Here, this issue is addressed by introducing orthonormal curves. In addition, utilizing thresholding in combination with active contouring, and automatically detecting the opening and closing frames, helped to minimize the number of frames that are incorrectly not processed in each cycle.

### 4.2.5 Impact of Frame Rate

Videos recorded at rates lower than 1000 fps typically yield blurry edges, which may impede processing. In fact, none of the methods of comparison (reference method, OAS and the original developed algorithm, OLFED) are able to cope with videos at frame rates such as 250 or even 500 fps as they are unable to find and properly process an ROI. Figure 4.11 shows the impact of the frame rate on image blurriness caused by the fast movement of the leaflets in the opening stage, with sample frames extracted from the variable quality subset of videos. High-quality videos at 1000 fps may not always be available due to the required specialized hardware, or for memory or storage space considerations. Thus, it is important to ensure that orifice segmentation algorithms work properly at lower frame rates.

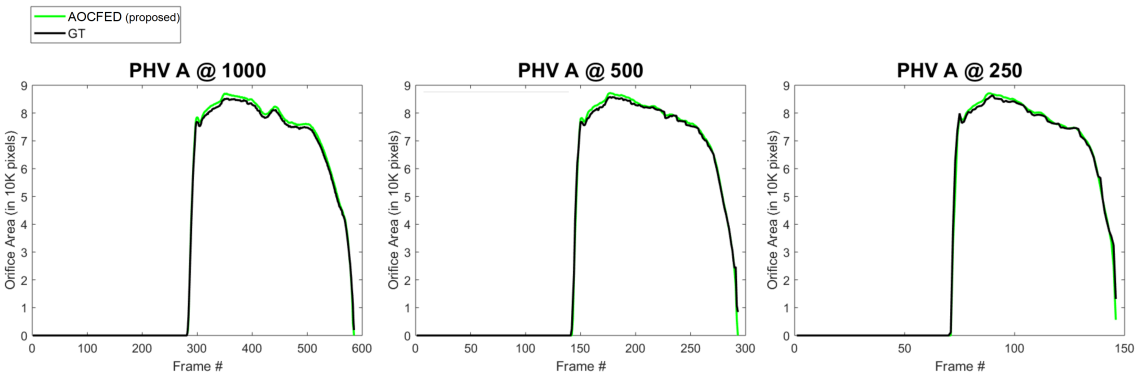


Figure 4.12: Comparison of the extracted orifice areas over time by our proposed approach (AOCFED) with the ground truth data (GT), for three different frame rates.

Figure 4.12 shows the orifice area over time for three different frame rates (videos PHV A @1000, PHV A @500, and PHV A @250). The results are in very good agreement with the GT, both in terms of curve shape and area, at all frame rates. One may note, looking at the GT (black curves in Figure 4.12), that the orifice area curves slightly differ across the videos with different frame rates while the valve is open. Even if recording the valve movements at slower frame rates decreases the accuracy of the data, the proposed method still finds orifice area profiles matching that of the GT.

Once again, valve design evaluation and computer vision metrics are used to assess the accuracy of the segmented orifice shape. First the orifice curves are compared and then the Jaccard similarity coefficient and Hausdorff distance values are presented (Table 4.5).

The RMSE values computed from the differences with the GT (Table 4.5) show that error increases as the frame rate decreases. The proposed method, when applied to the lowest quality video (250 fps), still outperforms the methods of comparison applied to the highest quality video (1000 fps) by 4.2 p.p. (OAS) and 1.2 p.p. (OLFED) (see also Table 4.2). Table 4.5 also shows the average Jaccard similarity coefficients over all frames between the GT and the orifice extracted by the proposed approach. One may note that the similarity to the GT tends to decrease slightly with the frame rate, but nevertheless remains acceptable and higher than that of the methods of comparison at the high frame rate, even at 250 fps, by 0.068 or 6.8 p.p. (OAS) and 0.012 or 1.2 p.p. (OLFED) (see Table 4.3).

The average $d_H$ over all frames between the GT and the orifice boundaries extracted by our proposed approach is also presented. The distance tends to increase slightly as the frame rate decreases but remains below that of the methods of comparison at the high frame rate, even at 250 fps, by 7.1 pixels (OAS) and 2.1 pixels

(OLFED) (see Table 4.4). Lower frame rate videos lack a sharp, strong, and bright edge—on which our proposed method relies—making them more susceptible to incorrect detections and consequently, to larger errors and distances and smaller similarity values. In spite of this, the proposed method, when applied to lower quality videos, still outperforms the methods of comparison applied to high quality videos.

Table 4.5: Measures of similarity between ground truth and the proposed approach (AOCFED) for three different frame rates. The measures include: RMSE values of the extracted orifice areas both absolute (in pixels) and relative (to the maximal orifice area), average Jaccard similarity coefficient (IoU) (± standard deviation), and average Hausdorff distance $d_H$ (± standard deviation)

| Measure | PHV A @ 1000 fps | PHV A @ 500 fps | PHV A @ 250 fps |
|---|---|---|---|
| RMSE | 1035 (1.2%) | 1149 (1.3%) | 1527 (1.8%) |
| IoU | 0.953 ± 0.094 | 0.945 ± 0.125 | 0.939 ± 0.132 |
| $d_H$ | 9.8 ± 13.1 | 10.8 ± 11.6 | 11.9 ± 10.5 |

## 4.3 Conclusion

In this chapter, several adjustments to the initially developed algorithm for quantitative performance analysis of biological PHVs were presented. The proposed refinements enhance the accuracy of the detected free edge of leaflets and successfully address the issue of the valve orifice being partly occluded by the inner side of the leaflets. The orifice area is first estimated via a mix of active contouring and thresholding and then refined via a contour transformation mechanism utilizing orthonormal curves, allowing the method to successfully segment the orifice area for valve design evaluation purposes. Automatic and precise determination of the beginning of the opening phase also helps to maximize the number of frames (in a cycle) that are accurately selected and processed. While selecting the frames, missing the frames

in the open phase of the cycle, and including the ones in the close cycle are both unwanted. The proposed method is successful in minimizing the number of unwanted frames, which could be very helpful in determining some malfunctions in the valve in the design stage.

A quantitative assessment on videos of three different valves demonstrated the approach's effectiveness to detect the leaflet free edges and thus obtain the actual orifice area during a complete cycle. The proposed approach outperformed a reference algorithm, as well as the original developed algorithm, both in terms of valve design evaluation metrics (accuracy of the temporal orifice area curves) and computer vision evaluation metrics (accuracy of the orifice shape). Experiments on the influence of the frame rate also demonstrated the robustness of our approach to varying recording speeds and the consequential blurriness of the leaflets in the videos. This increased accuracy of the results can translate into more accurate analyses of the valve's performance, especially in the valve design stage. The accurate detection of the contours of the leaflet free edges allows for the evaluation of several other important characteristics of the valve's motion and structure, such as fluttering and symmetry analysis. It also allows for determining whether leaflet edges ever come in contact with the stent of the valve, another important factor to consider in valve design.

In the next chapter, the contour of the detected free edges will be used for motion symmetry analysis of the PHVs and its potential correlation with functional symmetry and durability of the valve will be investigated.

# Chapter 5

# Visual Symmetry Analysis and Durability Estimation

Prosthetic heart valves replacement procedures are routinely used to replace defective native heart valves in patients suffering from valvular heart disease, with around 120000-180000 procedures performed yearly worldwide [58]. PHVs are not as mechanically robust as the mechanical valves and are proven to be less durable, especially in younger patients [55]. In fact more than 50% of them encounter a structural failure within 15 years post-implantation [72]. With tears and calcification being responsible for a majority of the failures [72, 79]. Tears on the valve leaflets mostly happen in areas under highly localized mechanical forces due to functional non-uniformities and asymmetries.

In this chapter, the correlation between the visual symmetry of PHVs in motion and their functional symmetry performance is investigated. The goal is to pave the way for utilizing computer vision techniques to estimate the durability of PHVs. The focus is on aortic PHV designs, which contain three symmetric leaflets. Figure 1.4 shows example frames of high-quality videos taken during *in vitro* pulsatile flow tests,

at various moments in the cardiac cycle.

Pulsatile flow tests are typically carried out during the valve design process to assess its performance via mechanical simulations of the cardiac flow (see Section 5.2.1). Fluid dynamics parameters and high quality imagery data are typically collected on these devices. Here, the symmetry of the valve's opening and closing patterns at the leaflet level is investigated by analyzing the contour of detected free edges of valve leaflets. This study aims to show that an asymmetry in the motion of each leaflet, compared to that of other leaflets, leads to differences in stress and forces on each leaflet (increased in some cases), which can affect the durability of the valve. For this purpose, in Section 5.1, two computer vision-based symmetry scores are proposed and defined to quantify the potentially existing asymmetry in the leaflets. Also, a numerical simulation of the valves in motion is performed to investigate the functional symmetry of the valve. To study the link between visual and functional symmetry, the results of symmetry analysis and numerical modeling of the valves are presented and compared in Section 5.2.

## 5.1 Proposed Method

Figure 5.1 shows the proposed method's flowchart, divided into two streams: CV-based analysis (top), and numerical modeling (bottom), converging in the end to show the correlation between visual and functional symmetry. For the CV stream, the contour of the valve orifice region (potentially derived from the developed algorithms in previous chapters), obtained from high-quality videos recorded during *in vitro* pulsatile flow tests and input to the system for each frame, is divided into three leaflet curves. The leaflet curves are then used for pair-wise motion symmetry analysis via the computation of two symmetry scores: DOPM and DTW. For the numerical

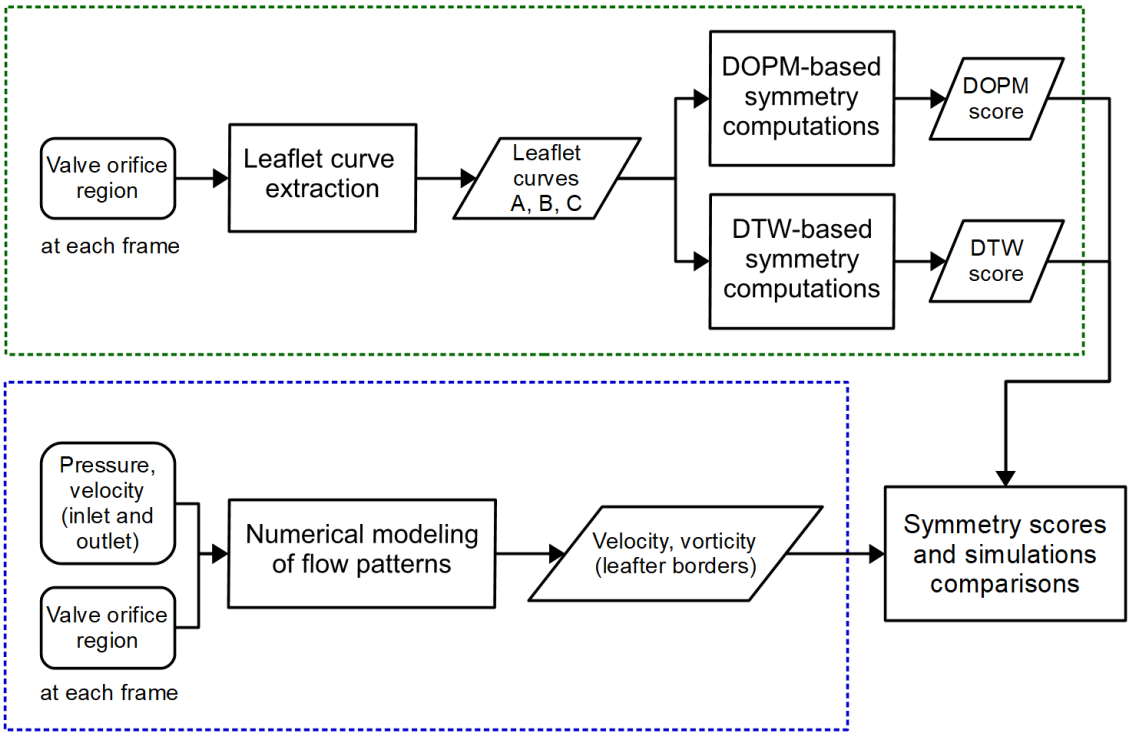


Figure 5.1: Flowchart of the proposed method. The three leaflet curves of the tricuspid valves are extracted from video data (valve orifice region) and their pairwise symmetry is analyzed via two different scores (DOPM and DTW). The score profiles are then compared to the results of numerical simulations to validate the link between visual symmetry and functional symmetry.

modeling stream, numerical simulations of the flow patterns during the cardiac cycle are conducted to estimate the amount of stress and forces on the leaflets. The simulations make use of the valve orifice region and of measured velocity and pressure data obtained during *in vitro* pulsatile flow tests as input, and output velocity and vorticity values at the leaflet borders. Finally, the symmetry scores are compared with the simulation results to assess their similarity.

### 5.1.1 Leaflet Curve Extraction

To evaluate the existing symmetry between the leaflets of a PHV, three pair-wise leaflet groups are considered, which yield three cases of bilateral symmetry. This

allows us to analyze the valve symmetry at the leaflet level and determine which leaflet, if any, causes an asymmetry in the valve orifice region during the cardiac cycle. This process is carried out for each frame of the pulsatile flow test video.

The binary mask of the valve orifice region is used as input to the leaflet curve extraction step (Figure 5.2 b). This mask can be obtained by the developed methods (described in previous chapters), via one of the valve orifice segmentation methods from the literature (e.g., [17, 27]), or from ground truth data. In this study, the latter option, the semi-automatic ground-truthing approach of [2] is selected, to discard any valve orifice segmentation error that would impact the evaluation of the proposed method. The contour of the valve orifice region (Figure 5.2 c) corresponds to the leaflet boundaries. For symmetry analysis purposes, one need to identify which part of the contour corresponds to each of the three leaflets. Here, this split is based on the location of the anchor points (Figure 5.2 a) and the valve center, found as described in section 3.1.1 (Figure 3.3). The contour is then split into three segments (leaflet curves) at the anchor points (Figure 5.2 d). The line passing through the anchor point common to two leaflets and the valve center is used later on as the symmetry axis for bilateral symmetry analysis, and for reflecting a leaflet curve and superimposing it on the other leaflet curves. The three leaflet curves are used to calculate the two symmetry scores as explained next.

### 5.1.2 DOPM-Based Symmetry

DOPM, reviewed in Section 2.3.2 , has been used for contour matching and for the detection of reflection symmetry. Using edge information, it relies on the curvature of two curves to evaluate their symmetry. It has been shown to be affine invariant and appropriate in the context of capturing structure-based patterns, which is desirable here.

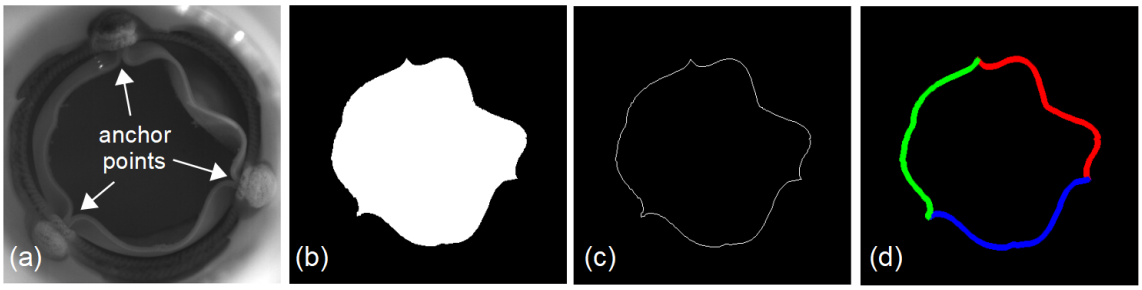


Figure 5.2: Leaflet curve extraction. (a) original frame, (b) valve orifice region mask, (c) contour of the valve orifice region, and (d) three extracted leaflet curves shown in green, red, and blue.

DOPM is based on the concept of edge fragments, or leaflet curve fragments in this case. An edge fragment $E_i$ on a curve is defined around an edge point $\boldsymbol{X}_i$ on the curve:

$$E_i = [\boldsymbol{X}_{i-n}, ..., \boldsymbol{X}_i, ..., \boldsymbol{X}_{i+n}]^T \tag{5.1}$$

where $X_i^T = [x_i, y_i]$ represents the edge point Cartesian coordinates. The edge fragment is thus the $n$-neighborhood of the edge point (here $n = 10$ is chosen by taking into account the length of the leaflet curves). The centerized configuration matrix $\breve{E}_i$ is introduced to move this edge fragment $E_i$ to the origin and remove translation effects:

$$\breve{E}_i = (I - \frac{1}{n}\mathbf{1}_n\mathbf{1}_n^T)E_i, \tag{5.2}$$

where $I$ is the identity matrix and $\mathbf{1}_n \coloneqq [1, ..., 1]^T \in \mathbb{R}^n$.

As its name suggests, the DOPM descriptor $W_{E_i}$ is then computed from Eq. (5.2) as the diagonal of the orthogonal projection matrix:

$$W_{E_i} = \text{diag}(\Pi_{\breve{E}_i})^{\frac{1}{2}}, \tag{5.3}$$

where $\Pi_{\breve{E}_i}$ is the orthogonal projection matrix on the range space of $\breve{E}_i$. The similarity

metric $\gamma$ between the edge fragments of two leaflet curves $A$ and $B$ is defined as:

$$\gamma(\breve{E}_i^A, \breve{E}_i^B) \coloneqq \|W_{E_i^A} - W_{E_i^B}\|_1, \tag{5.4}$$

where $\|\cdot\|_1$ denotes the 1-norm of the subtracted vector. $\gamma$ is calculated for all the edge points on the leaflet curve $A$ and their corresponding match on the leaflet curve $B$. The final DOPM score is obtained as the average of all $\gamma$ values:

$$\text{DOPM score} = \frac{1}{p}\sum_{i=1}^{p}\gamma(\breve{E}_i^A, \breve{E}_i^B), \tag{5.5}$$

where $p$ is the length of the smaller of the two leaflet curves $A$ and $B$. One should note that the smaller the DOPM score value, the higher the symmetry. Large values indicate the presence of asymmetry.

In [84], as symmetry is assumed and must be located, the two curves involved have the same length. In this case study, symmetry is not assumed and the leaflet curves can be of different lengths, since they are the product of a 2D projection on the image plane of their 3D shape. The process for finding corresponding edge points from two leaflet curves is thus not trivial, therefore, the following matching scheme is proposed. Let us assume that leaflet curve $A$ is shorter than leaflet curve $B$. All points from $A$ will make it to the final list of matched points, whereas some points from $B$ will be discarded. The process starts with the first point on $A$, for which the DOPM descriptor (Eq. 5.3) is calculated. The DOPM descriptors are then calculated for the first $n$ points (search neighborhood) on $B$. The point on $B$ that yields the lowest $\gamma$ value is considered as the best match for the first point on $A$. To preserve monotonicity, the matched point on $B$ is considered as the point on the lower end of the search neighborhood for the next point. The DOPM score is computed for all frames of the cardiac cycle.

### 5.1.3 DTW-Based Symmetry

The second approach to measure the reflective symmetry between two leaflet curves is proposed based on the Dynamic Time Warping or DTW. DTW finds the optimal match between two curves that yields the minimum summation of the absolute distance between corresponding points. Let's consider two curves ($A$ and $B$) represented by the following:

$$A = (a_1, a_2, ..., a_n), B = (b_1, b_2, ..., b_m), \tag{5.6}$$

where $a_i$ and $b_j = [x_i, y_i]^T$ are the coordinates of the $i^{th}$ and $j^{th}$ points on $A$ and $B$, and $n$ and $m$ are the length of $A$ and $B$, respectively. The DTW algorithm finds all possible alignment paths between points $a_i$ and $b_j$ which satisfy the following conditions: 1) Boundary condition: the first and last points of the curves should be the first and last points of the aligned sequence, i.e. $a_1$ and $b_1$ should be paired together as well as $a_n$ and $b_m$. This, however, does not need to be their only match. 2) Monotonicity condition: the order of the points should be preserved, i.e. the order of the aligned indices is never descending.

The alignment path with the minimum summation of the absolute pairwise distances is considered as the optimal alignment path. The minimum summation value is used as the DTW score. Since a higher distance implies a larger discrepancy between curves, the smaller the DTW score value, the higher the symmetry. To calculate the DTW score between two leaflet curves in a way that takes into account reflection symmetry, we first need to superimpose them. The first leaflet is thus reflected about the symmetry axis of the leaflets' pair, which is the line passing through the common anchor point of the leaflets and the valve center. Figure 5.3 shows an example of the two leaflets (red and green) in one leaflet pair, their symmetry axis (yellow) and the reflected curve (blue) of the first leaflet. The DTW score between the two

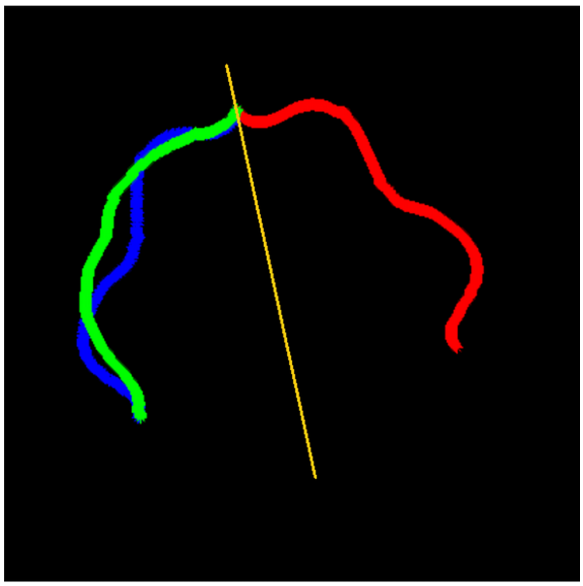

Figure 5.3: Superimposing the leaflet curves for the DTW score. The green and red leaflet curves are under examination for symmetry assessment, and the blue curve shows the reflection of the red curve about the symmetry axis (yellow line).

superimposed leaflet curves is calculated for each pair of leaflets and for all frames of the cardiac cycle.

### 5.1.4 Numerical Modeling of Flow Patterns

To investigate the correlation between the visual symmetry (analyzed via DOPM and DTW scores) and the functional symmetry (uniformity in the velocity and vorticity patterns found at the border of two leaflets), a numerical simulation of the valve in motion is performed. In the absence of a measured flow pattern at the leaflet borders, the goal is to confirm the possible impact of the valve opening asymmetries on the flow irregularities, which can lead to valve failure in the long term. The simulated values are observed throughout one cycle and their evolution is compared with that of the symmetry scores.

The proposed model is based on an open-source multi-physics solver (MPARS) [43, 70]. This solver is selected since in addition to being free and open-source, its

mesh-free Lagrangian numerical method lends itself to a natural handling of highly dynamic irregular immersed boundaries (here the heart valve), which are challenging for conventional mesh-based Eulerian methods [70]. The numerical model solves the conservation of mass (continuity) and momentum (Navier–Stokes) equations for incompressible flow in a Lagrangian framework:

$$\begin{cases} \frac{D\rho}{Dt} + \rho(\nabla \cdot \boldsymbol{u}) = 0 & \text{Continuity} \\ \rho\frac{D\boldsymbol{u}}{Dt} = -\nabla p + \mu\nabla^2\boldsymbol{u} + \boldsymbol{g} & \text{Momentum} \end{cases} \tag{5.7}$$

where $\rho$ is the fluid density, $\boldsymbol{u} : (u, v, w)$ is the fluid velocity vector in Cartesian coordinates $\boldsymbol{x} : (x, y, z)$, $p$ is the pressure, $\mu$ is the fluid dynamic viscosity, and $\boldsymbol{g}$ is the gravity vector. The numerical methods represent the computational domain with a set of free-to-move particles (nodes) over which Eqs. (5.7) are integrated (discretized) using a moving particle semi-implicit technique [70]. The time integration is via a predictor-corrector algorithm, and turbulence is modeled using a large eddy simulation model [70].

The simulations make use of pressure and velocity data measured at the inlet and outlet during *in vitro* pulsatile flow tests (as boundary conditions), and take into account the valve orifice region area available via the high-quality videos. They allow us to extract the velocity and vorticity fields at the leaflet borders. The velocity and vorticity give us the flow pattern (streamlines) as well as an indication of the shear stress, which are important cues for the evaluation of functional symmetry. The setup details are given in Section 5.2.2.

### 5.1.5 Symmetry Scores and Simulation Comparisons

Once DOPM and DTW score profiles are obtained with the CV stream and simulated velocity and vorticity profiles obtained with the numerical modeling stream over a

cardiac cycle, one need to find out how much they correlate. This comparison cannot focus on the values themselves since they are not representing the same variables. Instead, one can qualitatively investigate the overall trend and the location of the peaks in the graphs, and perform a quantitative difference-based comparison as follows.

The mean value of the graphs is first removed from all values; this centers the graphs around a value of 0. The graphs are then normalized (rescaled to the range [0, 1]), and the root-mean square error (RMSE) is calculated between the resulting graphs. Since there are three pairs of leaflets for each valve, there are three DOPM score profiles and three DTW score profiles that are each compared with the velocity and the vorticity profiles for each valve. This amounts to 12 comparisons per valve (6 scores x 2 simulated variables). One should note that the pair-wise velocity and vorticity profiles are computed as the absolute difference of the velocity and vorticity values at the border of the two leaflets involved.

## 5.2 Results and Discussion

### 5.2.1 Experimental setup and Video Dataset

As there are no public PHV video datasets available, a new dataset specific to this study is assembled. The experimental setup to collect high-quality videos and pressure and velocity data involves tricuspid PHVs mounted in the Pulse Duplicator device from ViVitro Labs [41]. The device reconstructs the performance of native heart valves by simulating the physiological cardiac conditions and flow patterns. Figure 5.4 shows the schematics of the heart anatomy and the device side by side, with arrows indicating which parts of the heart are modeled by each chamber of the device. Pressure ports and flow measuring sensors, located before and after the valve, are used to collect data that are input to the numerical modeling. The device uses an

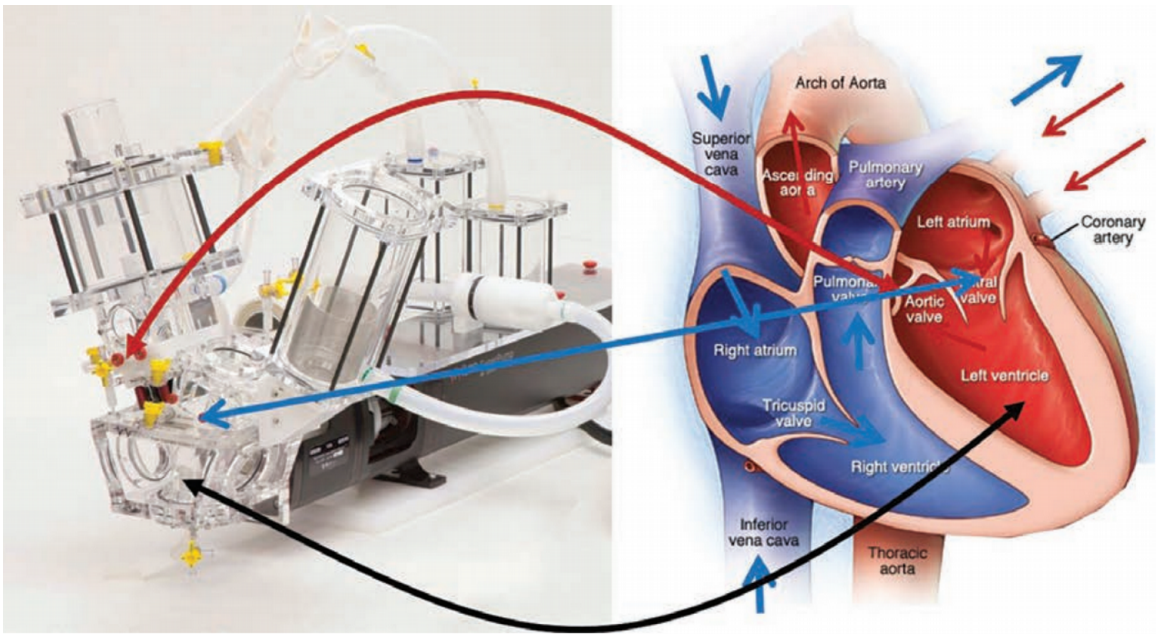


Figure 5.4: Pulse duplicator device (left) and schematic of the heart anatomy (right). Arrows show how each chamber of the device represents different parts of the heart, modeling the performance of the left side of the heart. The left chamber of the device is where PHVs are mounted (as aortic valves) and tested, and where the data are collected. Image from ViVitro Labs Inc.

anatomical model and a rigid anatomical aortic model with sinuses. The flow path is 28 mm in diameter. The inflow and outflow pressure transducers are located 65 mm and 85 mm from the midline of the valve, respectively. The midline of the electromagnetic flow probe is located 35 mm from the midline of the valve.

High-quality videos are captured during pulsatile tests and utilized as input to the CV processing. Videos are recorded for three different PHVs via a Photron SA3 highspeed digital camera, with a frame rate ranging from 250 to 1000 fps depending on the video, a shutter speed matching the frame rate, and a 300 ms test cycle, with resolutions between 400×400 and 1024×1024 pixels depending on the valve. Two of the PHVs (PHV-1 and PHV-2) are 25 mm in diameter, while the third is 19 mm (PHV-3). Two different test sessions are recorded for PHV-2, at 50 million cycles and at 200 million cycles. The dataset thus comprises four different experimental

cases with videos and the associated pressure and flow data: "PHV-1", "PHV-2-50", "PHV-2-200", and "PHV-3".

### 5.2.2 Numerical Setup

The computational domain is based on the Pulse Duplicator device with some simplifications. It includes a dynamic valve placed inside a 3D cylinder (Figure 5.5 a). To emulate a valve as genuinely as possible, the geometrical evolution of the valve orifice is taken directly from the real cases (not modeled). Since the only source for that information comes from the 2D camera imagery data providing projection of the actual 3D valve on the x-y plane, a 2D valve on the x-y plane perpendicular to the flow direction is simulated. Although this simplification may affect the flow pattern, the overall flow symmetries (and asymmetries) are expected to be reproduced. For each valve, an equivalent ideal valve is also simulated, with the orifice area equal to that of the actual valve but with a circular shape opening, providing an ideal symmetry. The results of those equivalent valves are used to remove the trends that are valve independent (e.g. boundary condition effects).

The working fluid is saline with a density of $\rho = 1000$ kg/m$^3$ and a viscosity of $\mu = 0.001$ Pa s. The boundary conditions include the measured velocity and pressure at the inlet and outlet, respectively (Figure 5.5 b). The domain is represented with a particle (node) size of $d_p = 0.035d$, where $d$ is the valve diameter ($d = 25$ mm in Figure 5.5 c, resulting in around 125,000 particles). A sensitivity analysis with respect to the particle size shows that smaller particle sizes would have an insignificant impact on the results. The time step size is automatically determined by the model to guarantee a stable solution. Figure 5.6 shows example flow simulations through a valve at different moments in the cardiac cycle, including snapshots of the simulation results (streamwise velocity component $w$, and streamline), and velocity time series at

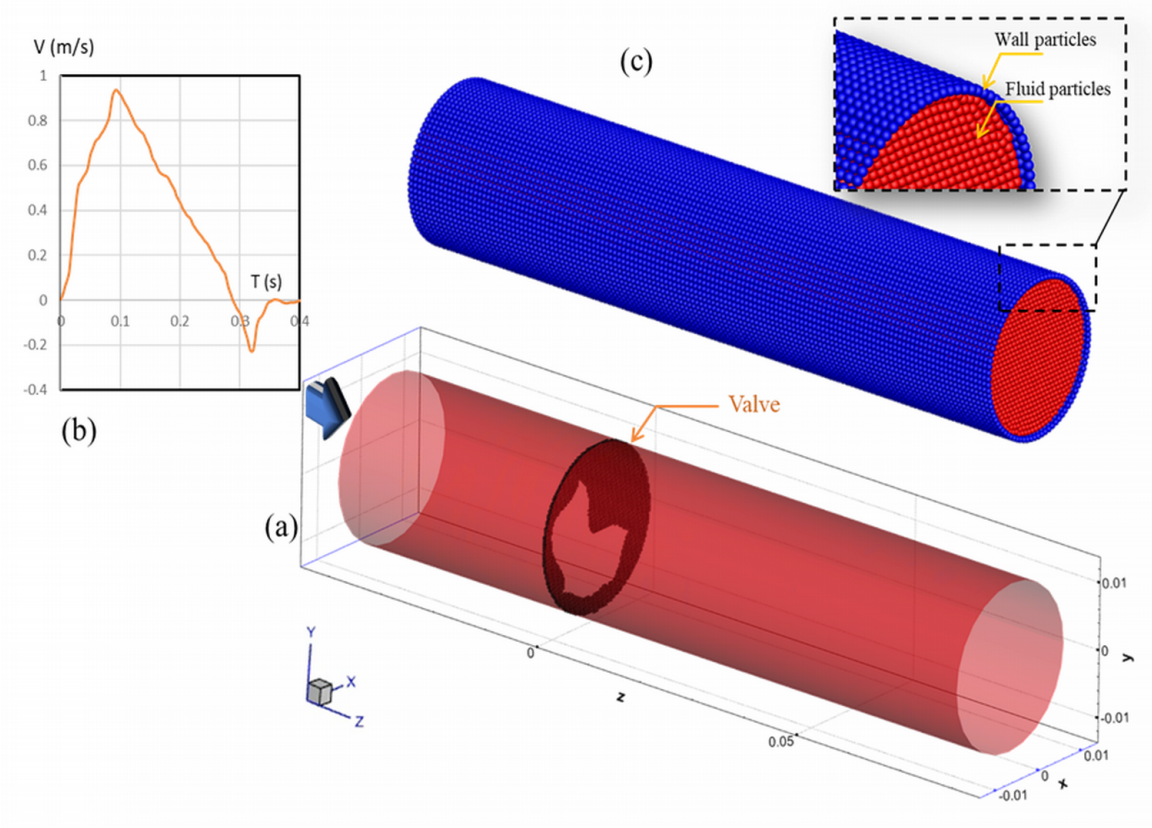


Figure 5.5: Numerical setup: (a) computational domain for a valve with a 25 mm diameter, (b) inlet boundary condition, i.e., known velocity time series, and (c) particle representation of the computational domain. The "Valve" tag indicates the profile of the orifice, obtained from the high-quality video.

three example points. Figure 5.7 shows examples of simulated vorticity and cross-wise (lateral) velocity magnitudes which are used for further comparisons.

### 5.2.3 Evaluation

Figure 5.8 shows the calculated pair-wise leaflet symmetry DOPM and DTW score profiles along with the simulated velocity and vorticity profiles for all four experimental cases. Qualitatively speaking, it is easy to see that the DTW score profiles (second column) are closer to the velocity (third column) and vorticity (fourth column) profiles than the DOPM score profiles (first column). Indeed, except for the PHV-1

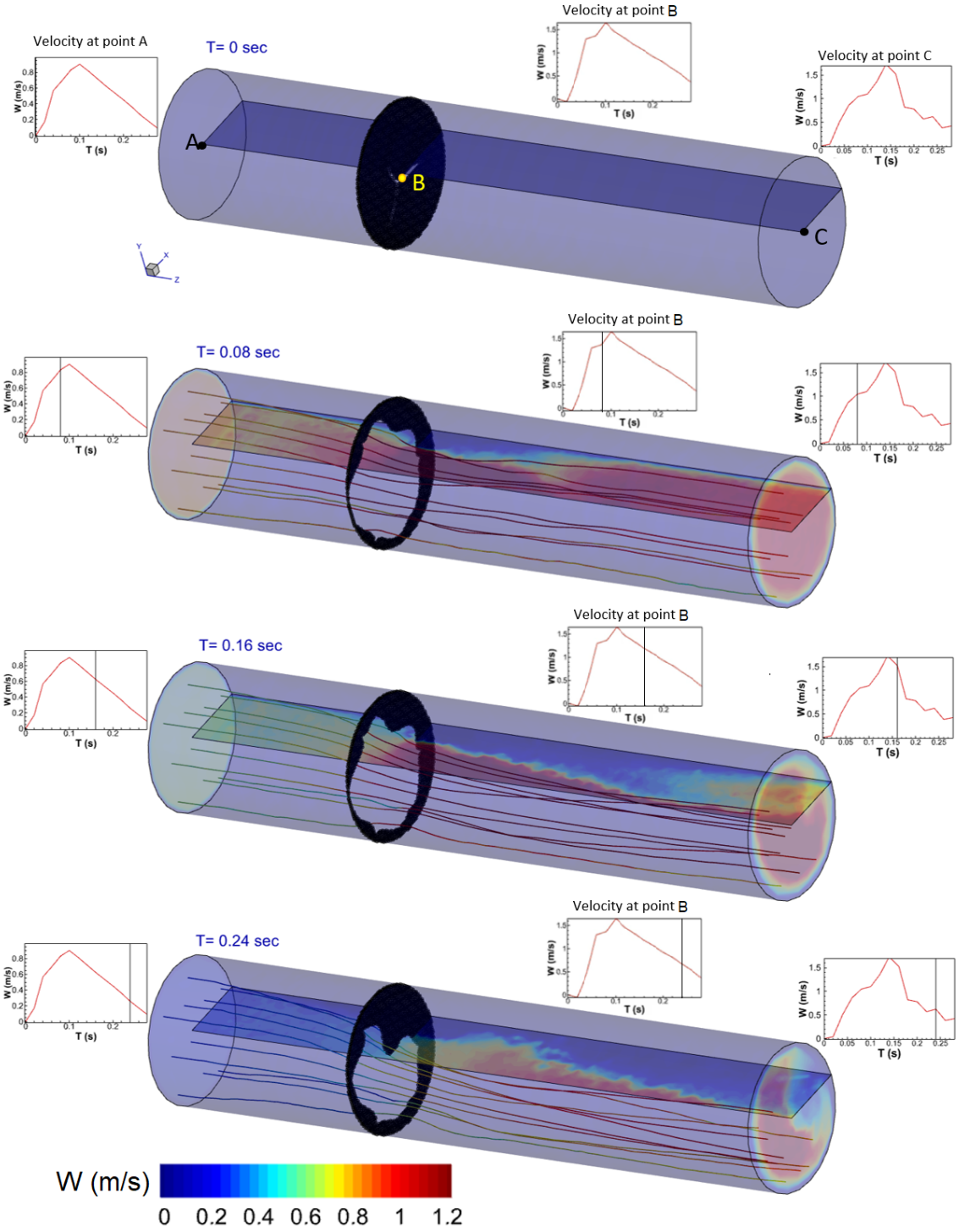


Figure 5.6: Example flow simulations through a valve, with a snapshot of the simulation results (streamwise velocity component $w$, and streamline), and velocity time series in points A, B and C.

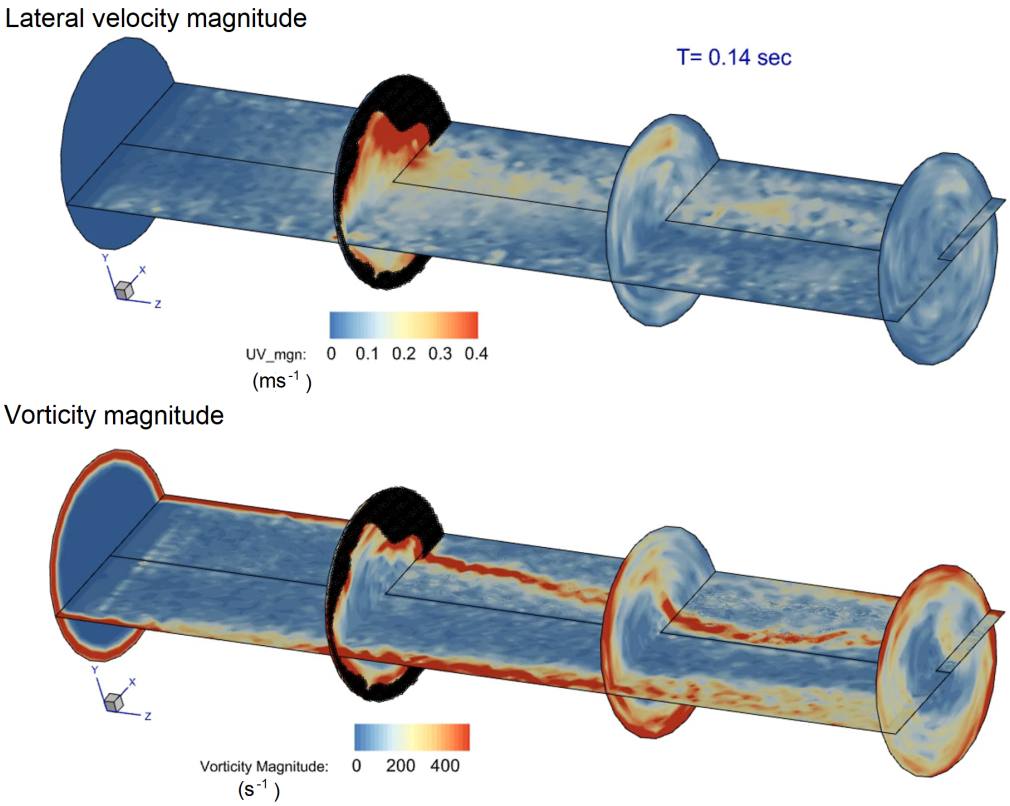


Figure 5.7: Example snapshots of simulated vorticity and lateral velocity magnitudes.

case, the global trend of the DOPM score profiles do not appear to follow that of the velocity and vorticity profiles. One possible explanation is that the DOPM score is computed locally, fragment by fragment, and summarized via averaging, whereas the DTW score is computed globally, which may be more appropriate in this case. One can see that the DTW score profiles' ranking of the symmetry among the three leaflet pairs generally follows that found in the velocity and vorticity profiles. For instance, for PHV-1, the $A\&C$ leaflet pair (in blue) is more visually symmetric than the other pairs, as is shown from the lower values in the DTW, velocity, and vorticity profiles; for PHV-2-50, this is seen for the $B\&C$ leaflet pair (in yellow), etc. The peaks in the DTW profiles generally correspond to the peaks in the velocity and vorticity profiles, e.g., around 15 ms and 280 ms for PHV-3. One can deduce from the DTW score

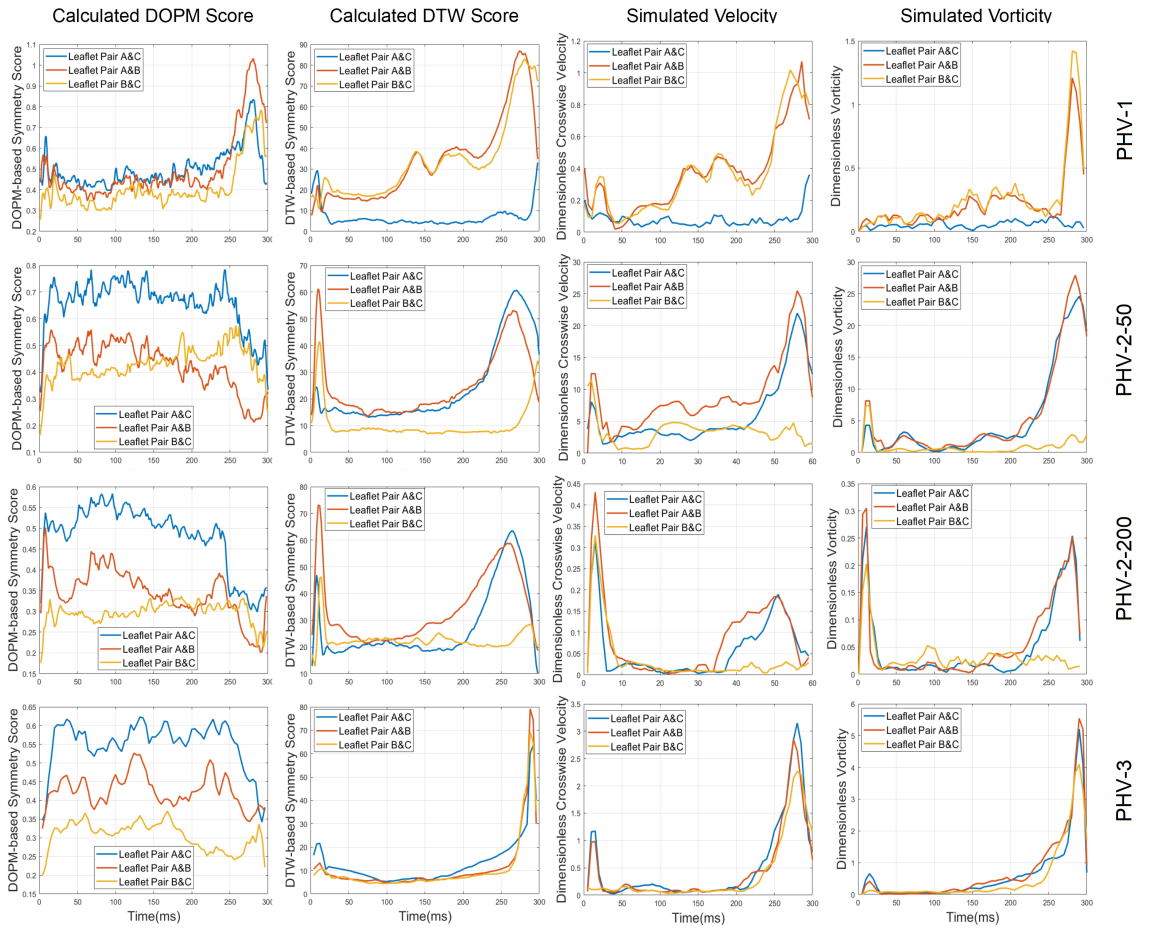


Figure 5.8: Calculated DOPM and DTW symmetry scores and simulated velocity and vorticity parameters for all four experimental cases.

profiles which leaflets cause asymmetries in the valve motion: for instance, looking at PHV-1 (first row, second column), leaflet $B$ is common to the two pairs involved in the largest scores, thus responsible for most asymmetries, which is confirmed by the $A\&C$ pair having the lowest score.

Figure 5.9 shows the DTW score profile for PHV-2-50 augmented with video frames and the corresponding valve orifice region mask at three key locations of the cardiac cycle. The scores are lower (more symmetry) when the valve is open, and higher (less symmetry) when the valve is opening and closing, as corroborated by the frames. Table 5.1 quantitatively compares the graphs of Figure 5.8. It presents the

| Case | Leaflet Pair | DOPM-Velocity | DOPM-Vorticity | DTW-Velocity | DTW-Vorticity |
|---|---|---|---|---|---|
| BHV-1 | A&B | 0.1642 | 0.1769 | 0.1288 | 0.2669 |
| | A&C | 0.3186 | 0.4497 | 0.1678 | 0.4525 |
| | B&C | 0.2067 | 0.1596 | 0.1044 | 0.2095 |
| BHV-2-50 | A&B | 0.9252 | 0.9622 | 0.2258 | 0.2663 |
| | A&C | 0.9696 | 1.0321 | 0.1713 | 0.1576 |
| | B&C | 0.4825 | 0.5371 | 0.2510 | 0.1603 |
| BHV-2-200 | A&B | 0.4533 | 0.5153 | 0.2152 | 0.2591 |
| | A&C | 0.8917 | 1.0330 | 0.2995 | 0.3412 |
| | B&C | 0.7257 | 0.6958 | 0.2024 | 0.1863 |
| BHV-3 | A&B | 0.6383 | 0.5755 | 0.2261 | 0.0899 |
| | A&C | 1.1504 | 1.1040 | 0.2322 | 0.0915 |
| | B&C | 0.7252 | 0.6761 | 0.1932 | 0.1003 |
| Average | | 0.6376 | 0.6598 | 0.2015 | 0.2151 |

Table 5.1: RMSE values of the calculated DOPM and DTW symmetry scores with respect to the simulated velocity and vorticity parameters for all four experimental cases.

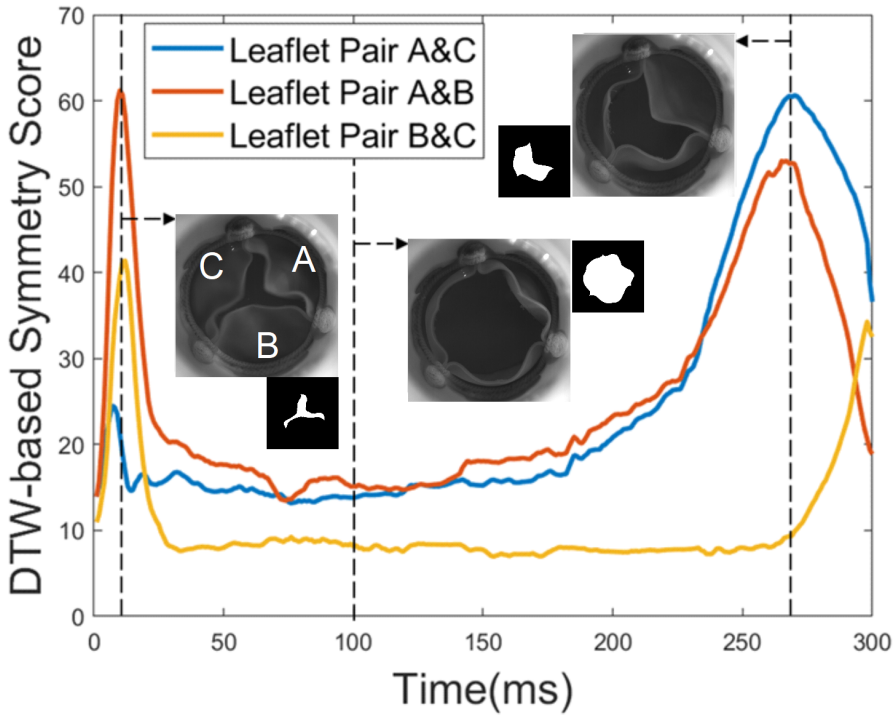


Figure 5.9: Calculated DTW symmetry score for PHV-2-250, showing frames from the high-quality video and the corresponding valve orifice region mask at three key locations of the cardiac cycle, from left to right: opening, open and closing phases.

RMSE values calculated between DOPM and DTW symmetry scores and simulated vorticity and velocity parameters. Lower RMSE values are preferable, with 0 indicating a perfect similarity of the graphs. On average, the RMSE values involving DTW are lower than those involving DOPM, which supports the observations on Figure 5.8. Regarding DOPM, PHV-1 yields the lowest RMSE values, which are comparable to those related to DTW. For the other cases, error values are too high for DOPM to be a reliable symmetry indicator. Regarding DTW, PHV-1 yields the lowest RMSE values for DTW-Velocity, whereas PHV-3 is showing the lowest error for DTW-Vorticity. Overall, DTW serves as a good indicator of valve functional symmetry due to its low error values, as low as 0.0899.

## 5.3 Conclusion

In this chapter it was shown that the visual symmetry of PHV leaflets is highly correlated with the functional symmetry of the valves. Visual reflection symmetry information, derived from the shape of pair-wise valve leaflet motion, is obtained from video data, acquired during pulsatile flow tests, via two different symmetry scores: DOPM and DTW. Functional symmetry information, related to physical values such as velocity and vorticity, is obtained via numerical simulations of the cardiac cycle, using actual data from pulsatile flow tests for the boundary conditions and effective valve orifice area. Experiments on four different cases that include three trileaflet PHVs of various diameters have shown that DTW score profiles are similar to the profiles of the velocity and vorticity at the leaflet borders, much more so than DOPM profiles. With RMSE values as low as 0.09, the DTW score constitutes a good indicator of the functional symmetry of the valve. This paves the way towards PHV durability estimations based on computer vision methods via symmetry analyses of the leaflet motion.

# Chapter 6

# Conclusions

## 6.1 Discussion

This dissertation proposed novel methods for the vision-based evaluation of prosthetic heart valves. Considering the fact that replacing defective native heart valves with prosthetic ones is a widely used practice, it is vital to ensure the prosthetics' reliability and durability before implantation. The evolution of the orifice area during a cardiac cycle, tracking of the free edge of leaflets, and the visual and functional symmetry of the valve are amongst the crucial quality evaluation metrics and of interest to this research study. The objective was to develop approaches for detecting the free edge of leaflets from high-speed videos, which consequently provides the orifice area of the valve. Chapters 3 and 4 present a novel segmentation approach, and critical refinements of it, respectively, along with a thorough experimental evaluation.

In Chapter 3, two algorithms were developed for segmentation of the orifice area and detection of the free edge of leaflets. They involved segmenting the opening of the valve using active contouring and then locating the borders of the leaflets by expanding and refining the segmented area. The comparison with a baseline approach

and with ground truth showed that the proposed methods are successful in tracking the free edge of leaflets. However, some drawbacks were also detected that needed to be addressed, including difficulties in locating the border of the leaflets in presence of the overly bright spots (e.g., close to the commission points), an undesirable number of unprocessed or inaccurately processed frames, and the need for high frame rate videos.

To overcome these challenges, several modifications were proposed in Chapter 4. This included a new approach for the generation of the initial mask (for active contouring) - which eliminated the need for high frame rate videos- and the trigger mechanism that enabled automatic and accurate detection of the beginning of the opening phase and consequently the closure of the valve at the end of the cardiac cycle. A combination of the thresholding and active contouring for more precise segmentation of the orifice area was also presented in addition to the use of orthonormal curves while expanding the segmented opening of the valve to better deal with the deformable characteristics of the leaflets and the excessively bright areas. The aggregation of the proposed adjustments to the initial algorithms resulted in a comprehensive method that is able to successfully and accurately detect and track the border of the leaflets in almost all the frames of a cardiac cycle in the presence of challenging illuminated areas and for videos with variable frame rates. Comparison of the results with those of the initial algorithm, the baseline method, and the ground truth showed that the developed algorithm, with the modifications in place, outperforms all the methods of comparison both in terms of valve design- and computer vision-related metrics.

The accurate detection of the border of leaflets provides the orifice area in each frame (orifice curve) , enabling us to study the evolution of the valve opening in a cycle. The orifice curve can also be used to assess other quality parameters such as opening and closing intervals, the maximum opening of the valve, when it happens,

and how long it stays open. Locating the free edge of leaflets also allows determining if the leaflets ever come in contact with the stent or surrounding area, after implantation, which is of interest for testing and authorizing the PHVs. In addition, precise determination of the beginning of the opening phase increases the number of processed frames in the opening and closing phases of the cardiac cycle, which is helpful in detecting some of the valve design malfunctions related to the improper closing of the PHVs.

In Chapter 5, to investigate the durability of PHVs using computer vision techniques, a correlation between visual symmetry and functional symmetry of the valves was hypothesized. The contour of the detected free edge of leaflets was used to derive visual reflection symmetry information of the valves in motion by defining two symmetry scores, DOPM and DTW. On the other hand, in order to evaluate the functional symmetry, numerical modeling of the valves was performed, and flow characteristics were extracted. Comparison of the defined symmetry scores and simulated results confirmed the correlation between visual asymmetries in motion of the leaflets and anomalies in flow patterns. Particularly, DTW symmetry score profiles were found to be in great agreement with variations of vorticity and crosswise velocity, which are the main sources of shear stress on the leaflets and accelerate the deterioration of the PHVs. By establishing such link between visual and functional symmetry of the heart valve, we paved the way for the durability estimation of the PHVs using computer vision methods.

## 6.2 Future Work

One of the challenges related to visual assessment of PHVs, to this day, is the absence of a public dataset. Should more visual data of different PHV designs and in various

stages of durability test be available, one could develop a unified symmetry measuring parameter that would allow for the comparison of different valves with different video characteristics (frame rates, resolution, etc.). DTW or such unified symmetry score could be used for categorizing and annotating videos of different valves and ultimately training deep learning networks to estimate PHV design durability based on visual symmetry in a more automated manner.

Potential future research works could also focus on generalizing the developed algorithms in this thesis to the visual data available from durability testing equipment (e.g., HiCycle Durability Tester from ViVitro) in order to evaluate the performance of prosthetic heart valves without the need to transfer them to the pulsatile flow devices. This could simplify the steps of examination and testing of the valve design before implantation. Such generalized approaches could also be applied to *in vivo* imagery data for assessing the performance of the prosthetic heart valves once they are implanted. The different nature of motion of leaflets in such durability testing equipment as well as varying angle of view for *in vivo* data are amongst the challenging factors that are needed to be considered in future work. The application of the developed methods could also be extended to other physiological studies such as detection and tracking of vocal folds in motion for the purpose of detecting abnormalities in laryngeal movements and environmental and meteorological studies where easily deformable materials (e.g., water, air, mud) are involved.

# Bibliography

[1] Cardiovascular diseases (cvds). http://www.who.int/cardiovascular_diseases/. Accessed: 2020-11-27.

[2] Retrieved from Heart and Stroke Foundation website. https://www.heartandstroke.ca/. Accessed: 2022-01-25.

[3] Somaya Adwan, Iqbal Alsaleh, and Rasha Majed. A new approach for image stitching technique using dynamic time warping (dtw) algorithm towards scoliosis x-ray diagnosis. *Measurement*, 84:32–46, 2016.

[4] Klaus Affeld, Peter Walker, and Klaus Schichl. The use of image processing in the investigation of artificial heart valve flow. *ASAIO Journal*, 35(3):294–298, 1989.

[5] Hee-Kap Ahn, Christian Knauer, Marc Scherfenberg, Lena Schlipf, and Antoine Vigneron. Computing the discrete fréchet distance with imprecise input. *International Journal of Computational Geometry & Applications*, 22(01):27–44, 2012.

[6] Maryam Alizadeh, Melissa Cote, and Alexandra Branzan Albu. Leaflet free edge detection for the automatic analysis of prosthetic heart valve opening and closing motion patterns from high speed video recordings. In *Scandinavian Conference on Image Analysis*, pages 15–27. Springer, 2017.

[7] Maryam Alizadeh, Melissa Cote, and Alexandra Branzan Albu. Automatic segmentation and tracking of biological prosthetic heart valves. *Journal of Medical Imaging*, 8(1):015501, 2021.

[8] Maryam Alizadeh, Melissa Cote, and Alexandra Branzan Albu. Towards durability estimation of bioprosthetic heart valves via motion symmetry analysis. In *Proceedings of the IEEE/CVF Winter Conference on Applications of Computer Vision*, pages 3124–3133, 2022.

[9] Helmut Alt, Christian Knauer, and Carola Wenk. Matching polygonal curves with respect to the fréchet distance. In *Annual Symposium on Theoretical Aspects of Computer Science*, pages 63–74. Springer, 2001.

[10] Armin Amindari, Levent Saltik, Kadir Kirkkopru, Magdi Yacoub, and Huseyin C Yalcin. Assessment of calcified aortic valve leaflet deformations and blood flow dynamics using fluid-structure interaction modeling. *Informatics in Medicine Unlocked*, 9:191–199, 2017.

[11] Ioannis Androulakis, Marguerite E Faure, Ricardo JP Budde, and Theo van Walsum. Automated quantification of bileaflet mechanical heart valve leaflet angles in CT images. *IEEE Transactions on Medical Imaging*, 2018.

[12] Mohamed-Salah Annabi, Erwan Salaun, Bernard Cosyns, Patrizio Lancellotti, and Philippe Pibarot. Multimodality imaging assessment of prosthetic aortic valve. In *Advances in Treatments for Aortic Valve and Root Diseases*, pages 95–123. Springer, 2018.

[13] Ibragim Atadjanov and Seungkyu Lee. Bilateral symmetry detection based on scale invariant structure feature. In *2015 IEEE International Conference on Image Processing (ICIP)*, pages 3447–3451. IEEE, 2015.

[14] Tim J Atherton and Darren J Kerbyson. Size invariant circle detection. *Image and Vision computing*, 17(11):795–803, 1999.

[15] Ch Brücker, U Steinseifer, W Schröder, and H Reul. Unsteady flow through a new mechanical heart valve prosthesis analysed by digital particle image velocimetry. *Measurement Science and Technology*, 13(7):1043, 2002.

[16] Kevin Buchin, Maike Buchin, and Yusu Wang. Exact algorithms for partial curve matching via the fréchet distance. In *Proceedings of the twentieth annual ACM-SIAM symposium on Discrete algorithms*, pages 645–654. SIAM, 2009.

[17] Alexander Burden, Melissa Cote, and Alexandra Branzan Albu. Fast and accurate rracking of highly deformable heart valves with locally constrained level sets. In *14th Conference on Computer and Robot Vision (CRV'17)*, pages 109–116. IEEE, 2017.

[18] Vikram Chalana and Yongmin Kim. A methodology for evaluation of boundary detection algorithms on medical images. *IEEE Transactions on Medical Imaging*, 16(5):642–652, 1997.

[19] T F Chan and L A Vese. Active contours without edges. *IEEE Transactions on Image Processing*, 10(2):266–277, 2001.

[20] Krishnan Bala Chandran and Srinivas Aluri. Mechanical valve closing dynamics: relationship between velocity of closing, pressure transients, and cavitation initiation. *Annals of Biomedical Engineering*, 25(6):926–938, 1997.

[21] Jie Chen, Shiguang Shan, Chu He, Guoying Zhao, Matti Pietikäinen, Xilin Chen, and Wen Gao. Wld: A robust local image descriptor. *IEEE Transactions on Pattern Analysis and Machine Intelligence*, 32(9):1705–1720, 2009.

[22] Fabien Chenot, Patrick Montant, Céline Goffinet, Agnès Pasquet, David Vancraeynest, Emmanuel Coche, Jean-Louis Vanoverschelde, and Bernhard L Gerber. Evaluation of anatomic valve opening and leaflet morphology in aortic valve bioprosthesis by using multidetector ct: comparison with transthoracic echocardiography. *Radiology*, 255(2):377–385, 2010.

[23] Minsu Cho and Kyoung Mu Lee. Bilateral symmetry detection via symmetry-growing. In *BMVC*, pages 1–11. Citeseer, 2009.

[24] Choeng Ryul Choi and Chang Nyung Kim. Numerical analysis on the hemodynamics and leaflet dynamics in a bileaflet mechanical heart valve using a fluid-structure interaction method. *ASAIO Journal*, 55(5):428–437, 2009.

[25] Marcelo Cicconet, David GC Hildebrand, and Hunter Elliott. Finding mirror symmetry via registration and optimal symmetric pairwise assignment of curves: Algorithm and results. In *Proceedings of the IEEE International Conference on Computer Vision Workshops*, pages 1759–1763, 2017.

[26] Alexandru Paul Condurache, Tobias Hahn, Ulrich G Hofmann, Michael Scharfschwerdt, Martin Misfeld, and Til Aach. Automatic measuring of quality criteria for heart valves. In *Medical Imaging 2007: Image Processing*, volume 6512, page 65122Q. SPIE, 2007.

[27] Alexandru Paul Condurache, Tobias Hahn, Michael Scharfschwerdt, Alfred Mertins, and Til Aach. Video-based measuring of quality parameters for tricuspid xenograft heart valve implants. *IEEE Transactions on Biomedical Engineering*, 56(12):2868–2878, 2008.

[28] Stéphane Derrode and Faouzi Ghorbel. Shape analysis and symmetry detection in gray-level objects using the analytical fourier–mellin representation. *Signal Processing*, 84(1):25–39, 2004.

[29] Pascal M Dohmen, Alexander Lembcke, Sebastian Holinski, Axel Pruss, and Wolfgang Konertz. Ten years of clinical results with a tissue-engineered pulmonary valve. *The Annals of Thoracic Surgery*, 92(4):1308–1314, 2011.

[30] Joseph R Dolensky, Lauren DC Casa, Andrew W Siefert, and Ajit P Yoganathan. In vitro assessment of available coaptation area as a novel metric for the quantification of tricuspid valve coaptation. *Journal of biomechanics*, 46(4):832–836, 2013.

[31] M-P Dubuisson and Anil K Jain. A modified hausdorff distance for object matching. In *Proceedings of 12th international conference on pattern recognition*, volume 1, pages 566–568. IEEE, 1994.

[32] Maximilian Eder, Fee v Waldenfels, Alexandra Swobodnik, Markus Klöppel, Ann-Kathrin Pape, Tibor Schuster, Stefan Raith, Elena Kitzler, Nikolaos A Papadopulos, Hans-Günther Machens, et al. Objective breast symmetry evaluation using 3-d surface imaging. *The Breast*, 21(2):152–158, 2012.

[33] L Henry Edmunds Jr. Thrombotic and bleeding complications of prosthetic heart valves. *The Annals of Thoracic Surgery*, 44(4):430–445, 1987.

[34] Sven Friedl, Eugen Herdt, Stefan König, Michael Weyand, Markus Kondruweit, and Thomas Wittenberg. Determination of heart valve fluttering by analyzing pixel frequency. In *Bildverarbeitung für die Medizin 2012*, pages 87–91. Springer, 2012.

[35] Sven Friedl, Stefan König, Markus Kondruweit, and Thomas Wittenberg. Digital kymography for the analysis of the opening and closure intervals of heart valves. In *Bildverarbeitung für die Medizin 2011*, pages 144–148. Springer, 2011.

[36] Sven Friedl, Stefan König, Michael Weyand, Thomas Wittenberg, and Markus Kondruweit. Dynamic heart valve cusp bending deformation analysis. In *Bildverarbeitung für die Medizin 2013*, pages 247–252. Springer, 2013.

[37] Zhi B Gao, Samir Pandya, Nadeen Hosein, Michael S Sacks, and Ned HC Hwang. Bioprosthetic heart valve leaflet motion monitored by dual camera stereo photogrammetry. *Journal of Biomechanics*, 33(2):199–207, 2000.

[38] Mauro Grigioni, Carla Daniele, Giuseppe D'avenio, Umberto Morbiducci, Costantino Del Gaudio, Mara Abbate, and David Di Meo. Innovative technologies for the assessment of cardiovascular medical devices: State-of-the-art techniques for artificial heart valve testing. *Expert Review of Medical Devices*, 1(1):81–93, 2004.

[39] Jesse Habets, Willem PTM Mali, and Ricardo PJ Budde. Multidetector CT angiography in evaluation of prosthetic heart valve dysfunction. *Radiographics*, 32(7):1893–1905, 2012.

[40] Tobias Hahn, Alexandru Paul Condurache, Til Aach, Michael Scharfschwerdt, and Martin Misfeld. Automatic in-vitro orifice area determination and fluttering analysis for tricuspid heart valves. In *Bildverarbeitung für die Medizin 2006*, pages 21–25. Springer, 2006.

[41] ViVitro Labs Inc. Information about our Pulse Duplicator System. http://vivitrolabs.com/product/pulse-duplicator/. Accessed: 2021-08-11.

[42] Arun KS Iyengar, Hiroatsu Sugimoto, David B Smith, and Michael S Sacks. Dynamic in vitro quantification of bioprosthetic heart valve leaflet motion using structured light projection. *Annals of Biomedical Engineering*, 29(11):963–973, 2001.

[43] M. Jandaghian, A. Krimi, A.R. Zarrati, and A. Shakibaeinia. Enhanced weakly-compressible mps method for violent free-surface flows: Role of particle regularization techniques. *Journal of Computational Physics*, 434:110202, 2021.

[44] Morten O Jensen, Andrew W Siefert, Ikechukwu Okafor, and Ajit P Yoganathan. Measurement technologies for heart valve function. In *Advances in Heart Valve Biomechanics*, pages 115–149. Springer, 2018.

[45] Arash Kheradvar, Elliott M Groves, Craig J Goergen, S Hamed Alavi, Robert Tranquillo, Craig A Simmons, Lakshmi P Dasi, K Jane Grande-Allen, Mohammad RK Mofrad, Ahmad Falahatpisheh, et al. Emerging trends in heart valve engineering: Part ii. novel and standard technologies for aortic valve replacement. *Annals of Biomedical Engineering*, 43(4):844–857, 2015.

[46] Shripad Kondra, Alfredo Petrosino, and Sara Iodice. Multi-scale kernel operators for reflection and rotation symmetry: further achievements. In *Proceedings of the IEEE Conference on Computer Vision and Pattern Recognition Workshops*, pages 217–222, 2013.

[47] Markus Kondruweit, Sven Friedl, Christian Heim, Thomas Wittenberg, Michael Weyand, and Frank Harig. A new ex vivo beating heart model to investigate the application of heart valve performance tools with a high-speed camera. *Asaio Journal*, 60(1):38–43, 2014.

[48] Markus Kondruweit, Sven Friedl, Thomas Wittenberg, René Tandler, and Michael Weyand. Description of a novel ex-vivo imaging and investigation technique to record, analyze and visualize heart valve motions under physiological conditions. *Heart, Lung and Circulation*, 19:S174, 2010.

[49] Trung Bao Le and Fotis Sotiropoulos. Fluid-structure interaction simulation of an aortic bi-leaflet mechanical heart valve in a patient-specific left heart. In *5th Biennial Conference on Heart Valve Biology and Tissue Engineering*, volume 2012, page 51. Hamad bin Khalifa University Press (HBKU Press), 2012.

[50] Mark N Levine, Gary Raskob, and Jack Hirsh. Hemorrhagic complications of long-term anticoagulant therapy. *Chest*, 95(2):26S–36S, 1989.

[51] Yanxi Liu, Hagit Hel-Or, Craig S Kaplan, and Luc Van Gool. *Computational symmetry in computer vision and computer graphics*. Now publishers Inc, 2010.

[52] Gareth Loy and Jan-Olof Eklundh. Detecting symmetry and symmetric constellations of features. In *European Conference on Computer Vision*, pages 508–521. Springer, 2006.

[53] Po-Chien Lu, Jia-Shing Liu, Ren-Hong Huang, Chi-Wen Lo, Ho-Cheng Lai, and Ned HC Hwang. The closing behavior of mechanical aortic heart valve prostheses. *Asaio Journal*, 50(4):294–300, 2004.

[54] Rizwan A Manji and Jacqueline S Manji. Studying xenograft rejection of bioprosthetic heart valves. In *Xenotransplantation*, pages 227–243. Springer, 2020.

[55] Aldo Milano, Cosimo Guglielmi, Marco De Carlo, Omar Di Gregorio, Giancarlo Borzoni, Francesco Verunelli, and Uberto Bortolotti. Valve-related complications in elderly patients with biological and mechanical aortic valves. *The Annals of Thoracic Surgery*, 66(6):S82–S87, 1998.

[56] Hadi Mohammadi and Kibret Mequanint. Prosthetic aortic heart valves: modeling and design. *Medical Engineering & Physics*, 33(2):131–147, 2011.

[57] Piero Montorsi, Francesca De Bernardi, Manuela Muratori, Dario Cavoretto, and Mauro Pepi. Role of cine-fluoroscopy, transthoracic, and transesophageal echocardiography in patients with suspected prosthetic heart valve thrombosis. *The American Journal of Cardiology*, 85(1):58–64, 2000.

[58] Yosri S Morsi, Ian E Birchall, and Franklin L Rosenfeldt. Artificial aortic valves: an overview. *The International Journal of Artificial Organs*, 27(6):445–451, 2004.

[59] Hunter R Moyer, Grant W Carlson, Toncred M Styblo, and Albert Losken. Three-dimensional digital evaluation of breast symmetry after breast conservation therapy. *Journal of the American College of Surgeons*, 207(2):227–232, 2008.

[60] Andriy Myronenko and Xubo Song. Intensity-based image registration by minimizing residual complexity. *IEEE transactions on medical imaging*, 29(11):1882–1891, 2010.

[61] Vuyisile T Nkomo, Julius M Gardin, Thomas N Skelton, John S Gottdiener, Christopher G Scott, and Maurice Enriquez-Sarano. Burden of valvular heart diseases: a population-based study. *The Lancet*, 368(9540):1005–1011, 2006.

[62] Laura Pałys, Mirosław W Mrzygłód, Maciej Gawlikowski, and Roman Major. Optimization of inlet valve leaflet shape using metamodel and fluid-structure interaction. In *14th WCCM-ECCOMAS Congress 2020*, volume 400, 2021.

[63] Viorica Patraucean, Rafael Grompone von Gioi, and Maks Ovsjanikov. Detection of mirror-symmetric image patches. In *Proceedings of the IEEE Conference on Computer Vision and Pattern Recognition Workshops*, pages 211–216, 2013.

[64] Daniel Reisfeld and Yehezkel Yeshurun. Robust detection of facial features by generalized symmetry. In *International Conference on Pattern Recognition*, pages 117–117. IEEE Computer Society Press, 1992.

[65] Alexis Roche, Gregoire Malandain, and Nicholas Ayache. Unifying maximum likelihood approaches in medical image registration. *International Journal of Imaging Systems and Technology*, 11(1):71–80, 2000.

[66] Carlo Rostagno. Heart valve disease in elderly. *World Journal of Cardiology*, 11(2):71, 2019.

[67] Ethan Rublee, Vincent Rabaud, Kurt Konolige, and Gary Bradski. Orb: An efficient alternative to sift or surf. In *2011 International conference on computer vision*, pages 2564–2571. Ieee, 2011.

[68] Frederick J Schoen and Robert J Levy. Calcification of tissue heart valve substitutes: progress toward understanding and prevention. *The Annals of Thoracic Surgery*, 79(3):1072–1080, 2005.

[69] Kaveh Shahbaz. Applied similarity problems using fréchet distance. *arXiv preprint arXiv:1307.6628*, 2013.

[70] Ahmad Shakibaeinia and Yee-Chung Jin. A weakly compressible mps method for modeling of open-boundary free-surface flow. *International Journal for Numerical Methods in Fluids*, 63(10):1208–1232, 2010.

[71] Dinggang Shen, Horace Ho-Shing Ip, Kent KT Cheung, and Eam Khwang Teoh. Symmetry detection by generalized complex (gc) moments: a close-form solution. *IEEE Transactions on Pattern Analysis and Machine Intelligence*, 21(5):466–476, 1999.

[72] Raheela Fareed Siddiqui, Johnathan Rajiv Abraham, and Jagdish Butany. Bioprosthetic heart valves: modes of failure. *Histopathology*, 55(2):135–144, 2009.

[73] Grant Stearns, Neelakantan Saikrishnan, Andrew W Siefert, and Ajit P Yoganathan. Transcatheter aortic valve implantation can potentially impact short-term and long-term functionality: An in vitro study. *International Journal of Cardiology*, 172(3):e421–e422, 2014.

[74] Dominika Suchá, Petr Symersky, Wilco Tanis, Willem P Th M Mali, Tim Leiner, Lex A van Herwerden, and Ricardo PJ Budde. Multimodality imaging assessment of prosthetic heart valves. *Circulation: Cardiovascular Imaging*, 8(9):e003703, 2015.

[75] Petr Symersky, Ricardo PJ Budde, Bas AJM de Mol, and Mathias Prokop. Comparison of multidetector-row computed tomography to echocardiography and fluoroscopy for evaluation of patients with mechanical prosthetic valve obstruction. *The American Journal of Cardiology*, 104(8):1128–1134, 2009.

[76] Marie-Christine Taillefer, Gilles Dupuis, Jean-François Hardy, and Sylvie LeMay. Quality of life before and after heart valve surgery is influenced by gender and type of valve. *Quality of life Research*, 14(3):769–778, 2005.

[77] Demetri Terzopoulos and Kurt Fleischer. Deformable models. *The visual Computer*, 4(6):306–331, 1988.

[78] Ibrahim Turkoglu, Ahmet Arslan, and Erdogan Ilkay. An expert system for diagnosis of the heart valve diseases. *Expert systems with applications*, 23(3):229–236, 2002.

[79] Ivan Vesely. The evolution of bioprosthetic heart valve design and its impact on durability. *Cardiovascular Pathology*, 12(5):277–286, 2003.

[80] Ivan Vesely, Derek Boughner, and Tom Song. Tissue buckling as a mechanism of bioprosthetic valve failure. *The Annals of Thoracic Surgery*, 46(3):302–308, 1988.

[81] Florian von Knobelsdorff-Brenkenhoff, Matthias A Dieringer, Andreas Greiser, and Jeanette Schulz-Menger. In vitro assessment of heart valve bioprostheses by cardiovascular magnetic resonance: Four-dimensional mapping of flow patterns and orifice area planimetry. *European Journal of Cardio-Thoracic Surgery*, 40(3):736–742, 2011.

[82] Marija Vukićević, Stefania Fortini, Giorgio Querzoli, Stefania Espa, and Gianni Pedrizzetti. Experimental study of an asymmetric heart valve prototype. *European Journal of Mechanics-B/Fluids*, 35:54–60, 2012.

[83] Zhaozhong Wang, Min Liang, and Youfu Li. Using diagonals of orthogonal projection matrices for affine invariant contour matching. *Image and Vision Computing*, 29(10):681–692, 2011.

[84] Zhaozhong Wang, Zesheng Tang, and Xiao Zhang. Reflection symmetry detection using locally affine invariant edge correspondence. *IEEE Transactions on Image Processing*, 24(4):1297–1301, 2015.

[85] Thomas Wittenberg, Robert Cesnjevar, Stephan Rupp, Michael Weyand, and Markus Kondruweit. High-speed-camera recordings and image sequence analysis of moving heart-valves: Experiments and first results. In *Advances in Medical Engineering*, pages 169–174. Springer, 2007.

[86] Z Jon Wu, Ying Wang, and Ned H C Hwang. Occluder closing behavior: A key factor in mechanical heart valve cavitation. *The Journal of heart valve disease*, 3 Suppl 1:S25–33; discussion S33, 05 1994.

[87] Chenyang Xu, Dzung L Pham, and Jerry L Prince. Image segmentation using deformable models. *Handbook of medical imaging*, 2(20), 2000.

[88] Yihong Yuan and Martin Raubal. Extracting dynamic urban mobility patterns from mobile phone data. In *International conference on geographic information science*, pages 354–367. Springer, 2012.

[89] Rana Zakerzadeh, Ming-Chen Hsu, and Michael S Sacks. Computational methods for the aortic heart valve and its replacements. *Expert review of medical devices*, 14(11):849–866, 2017.

[90] Conrad M Zapañta, David R Stinebring, Steven Deutsch, David B Geselowitz, and John M Tarbell. A comparison of the cavitation potential of prosthetic heart valves based on valve closing dynamics. *Journal of Heart Valve Disease*, 7(6):655–667, 1998.